Journal of Sensors

High Sensitivity Electromagnetic Sensors and Their Applications

Lead Guest Editor: Dongfeng He
Guest Editors: Lalita Udpa, Xiangyan Kong, and Kai Wu

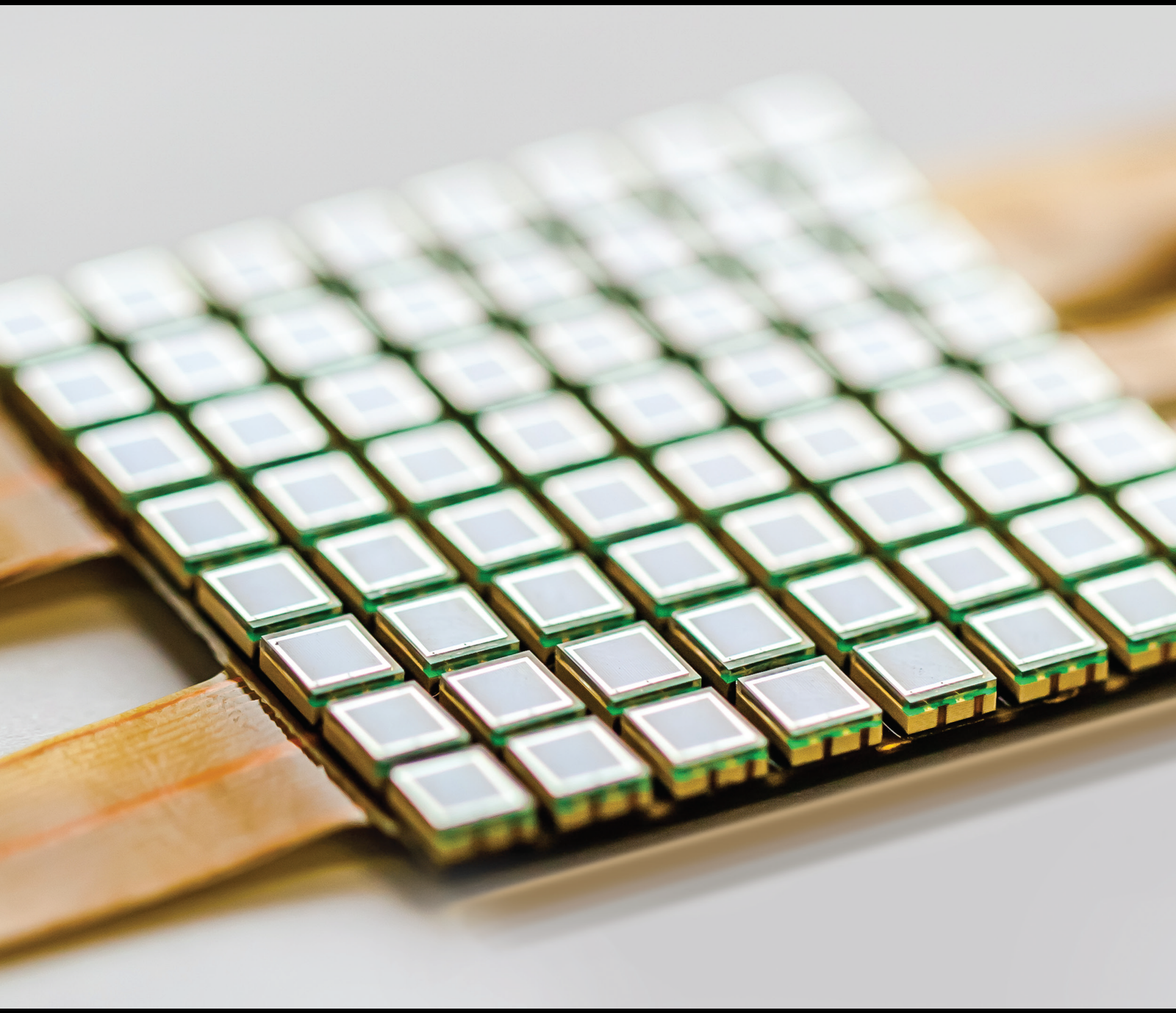

High Sensitivity Electromagnetic Sensors and Their Applications

Journal of Sensors

High Sensitivity Electromagnetic Sensors and Their Applications

Lead Guest Editor: Dongfeng He
Guest Editors: Lalita Udpa, Xiangyan Kong, and Kai Wu

Contents

Hindawi
Journal of Sensors
Volume 2019, Article ID 2413408, 8 pages
https://doi.org/10.1155/2019/2413408

Research Article

A Feedback Method to Improve the Dynamic Range and the Linearity of Magnetoimpedance Magnetic Sensor

Dongfeng He

National Institute for Materials Science, Tsukuba, Ibaraki 305-0047, Japan

Correspondence should be addressed to Dongfeng He; he.dongfeng@nims.go.jp

Received 20 August 2019; Accepted 11 November 2019; Published 12 December 2019

Academic Editor: Stelios M. Potirakis

We developed a high-sensitivity magnetoimpedance magnetic field sensor using a FeCoSiB amorphous wire and a coil wound around it. The amorphous wire had the diameter of 0.1 mm and the length of 5 mm. The magnetic field resolution of about 20 pT/$\sqrt{}$Hz was achieved. But the dynamic range of the magnetoimpedance magnetic field sensor was only about ±0.7 Gauss, which was not enough for some applications, such as the defect evaluation of steel plate. The linearity of the system was also not good when big magnetic field was applied, which will cause some noise when the system is used in unshielded environment. We developed a feedback method to improve the dynamic range and the linearity of the magnetic field sensor. The operation point of the magnetic field sensor was fixed by sending a feedback current to the coil. Using the feedback method, the dynamic range was improved from ±0.7 Gauss to ±10 Gauss and the linearity was also improved over 100 times better. An eddy current testing system using the magnetic sensor was developed, and the crack defects in steel plate and in 3D-printed titanium alloy plate were evaluated.

1. Introduction

Room temperature-sensitive magnetic sensors have been developed and used in various areas of communication, geological exploration, medical diagnostics, nondestructive evaluation (NDE), and security control [1–10]. These sensors are normally operated in unshielded environment with big background interferences, such as the power line interference. To measure the small signal in the big background interferences, good linearity of the sensing system is important. Otherwise, the big background interferences may cause the distortion of the signal and increase the noise of the system.

For the NDE application of magnetic sensor, some ferromagnetic material samples may produce strong magnetic fields and cause the saturation of the magnetic sensors. Feedback methods are often used to increase the dynamic ranges of magnetic sensors and improve the linearity of magnetic sensors [11–13].

Using the $(Fe_{0.06}Co_{0.94})_{72.5}Si_{12.5}B_{15}$ (FeCoSiB) amorphous wire with the diameter of 0.1 mm and the length of 5 mm, we developed a high-sensitivity magnetoimpedance (MI) sensor [14]. There was no electrical connection with the amorphous wire. The DC bias current and the AC current flow in the coil directly. In this paper, we present our new results of the high-sensitivity MI sensor and a feedback method to improve the dynamic range and the linearity of the magnetic sensing system. We also constructed the eddy current testing (ECT) system with the magnetic sensor and used it to evaluate the crack defect of 3D-printed titanium alloy and steel plate.

2. MI Magnetic Sensor without Feedback

Figure 1 shows the schematic block diagram of the MI magnetic field sensor made using the FeCoSiB amorphous wire and the driving circuit without feedback. The sensor element was composed of a FeCoSiB amorphous wire and a coil wound around it. Different from normal MI sensor, there was no electrical connection with the amorphous wire. To make it capable of measuring the applied DC magnetic field, DC bias current and AC bias current were used in the driving circuit. The inductor L_D and the capacitors of C1 and C2 were used to isolate the DC bias current, the AC bias current, and the voltage signal across the coil. The magnetic sensor is

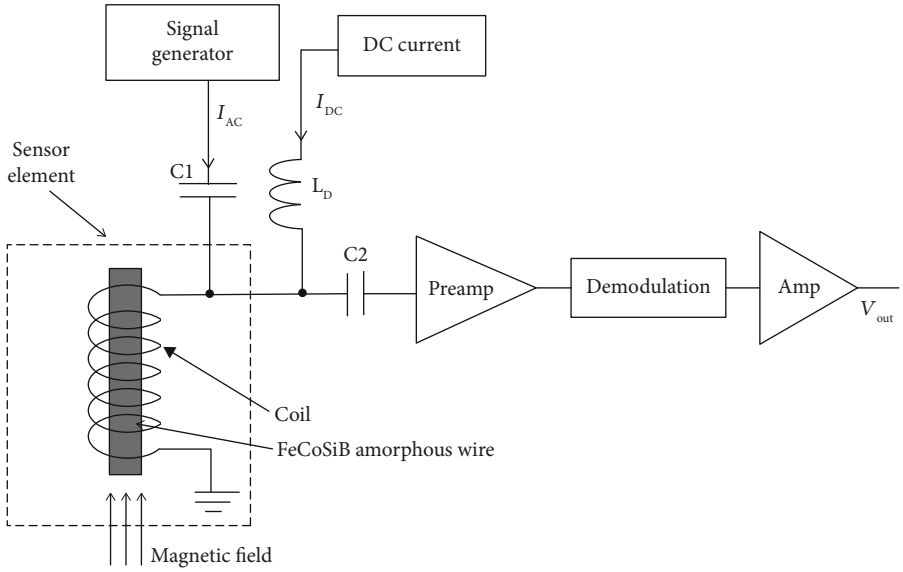

Figure 1: Schematic block diagram of the magnetic field sensor made using the FeCoSiB amorphous wire and the driving circuit without feedback.

used to measure the magnetic field along the direction of the amorphous wire.

In our experiments, the length of the FeCoSiB amorphous wire was 5 mm and the diameter was 0.1 mm. The coil wound around the amorphous wire was 30 turns wrapped using a copper wire with a diameter of 0.1 mm. The diameter of the coil was about 0.6 mm. The DC bias current was about 50 mA, and the amplitude of the AC bias current was about 20 mA. The frequency of the AC bias current ranged from 100 kHz to 5 MHz, and maximum signal amplitudes were achieved when the frequency was between 1 MHz and 2 MHz. In this paper, we used the frequency of 1 MHz.

Figure 2 shows the *B-H* curve of the FeCoSiB amorphous wire and the principle of the MI magnetic field sensor. The DC bias current I_{DC} in Figure 1 produced the DC magnetic field H_{DC}, and the AC bias current I_{AC} in Figure 1 produced the AC magnetic field H_{AC}, V_{AC} was the voltage across the coil wound around the amorphous wire. If H_{DC} was small, the sensor element operated in the linear part of the *B-H* curve, the amplitude of V_{AC} did not change with the external applied DC or low-frequency magnetic field. It could not be used to measure the DC magnetic field. If the DC bias current was increased and H_{DC} was near to the saturation corner of the *B-H* curve, the amplitude of V_{AC} changed with the external DC or low-frequency magnetic field.

Figure 3(a) shows the voltage signal when the external applied magnetic field was 0 Gauss. The signal amplitude was about 100 mV. Figure 3(b) shows the voltage signal when the external applied magnetic field was 1 Gauss. The signal amplitude was about 80 mV. The signal amplitude changed with the applied DC magnetic field.

In the driving circuit shown in Figure 1, the preamplifier with the gain of 30 dB was used to amplify the 1 MHz AC voltage signal. The demodulation was used to get the amplitude signal of the AC voltage signal, and the output voltage of V_{out} was used to measure the external DC or low-frequency magnetic field. We measured the output voltage changing with the applied external magnetic field. Figure 4 shows the results. For the applied external magnetic field between -0.7 Gauss and +0.7 Gauss, the magnetic field response of the magnetic sensor was nearly linear.

Figure 5 shows the magnetic field noise spectrum of the magnetic sensor with amorphous wire. The magnetic field noise spectrum was measured in a three-layer permalloy shielding box. The peaks on the spectrum were the 50 Hz inference and its harmonics. The magnetic field resolution of about 20 pT/$\sqrt{}$Hz was obtained.

To observe the distortion of the output signal of the magnetic field sensor, we applied a 30 Hz sine wave magnetic field to the sensor by putting the sensor in the centre of a Helmholtz coil, and the Helmholtz coil was connected with a 30 Hz sine wave current source. For the sensor without feedback, if the applied field was small and in the linear range of the magnetic field sensor, the distortion of the signal was small. Figure 6 shows the output signal when the amplitude of the 30 Hz applied magnetic field was 0.2 Gauss (0.02 mT). If the applied field was big and exceeded the linear range of the magnetic field sensor, the distortion of the signal was big. Figure 7 shows the output signal when the amplitude of the 30 Hz applied magnetic field was 2 Gauss (0.2 mT).

Figure 8 shows the spectrum of the output signal for the 30 Hz applied magnetic field with the amplitude of 2 Gauss. Due to the signal distortion, the amplitudes of the harmonics were quite big.

Total harmonic distortion (THD) is normally used to evaluate the nonlinearity of magnetic sensing systems [15–17]. When a sinusoidal magnetic field is applied to the magnetic sensor, the THD of the output signal can be defined

$$\mathrm{THD} = \frac{\sqrt{A_2^2 + A_3^2 + \cdots}}{A_1}, \quad (1)$$

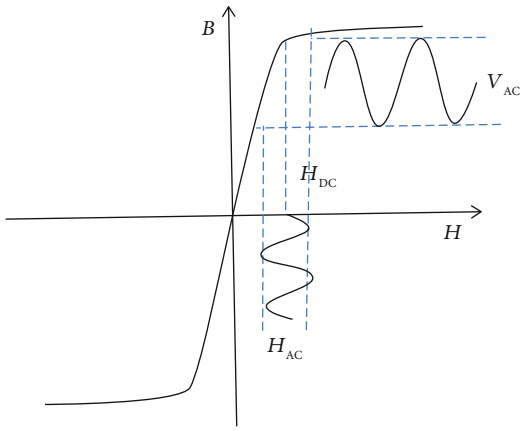

Figure 2: The *B-H* curve of the FeCoSiB amorphous wire and the principle of MI magnetic field sensor.

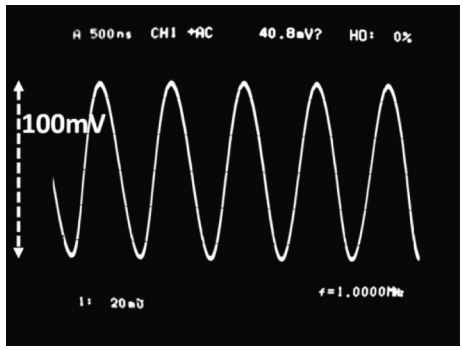

(a)

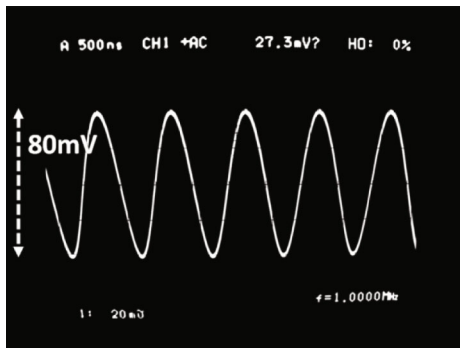

(b)

Figure 3: Voltage signal across the coil for different applied DC fields. (a) The signal when the applied field was zero. (b) The signal when the applied field was 1 Gauss.

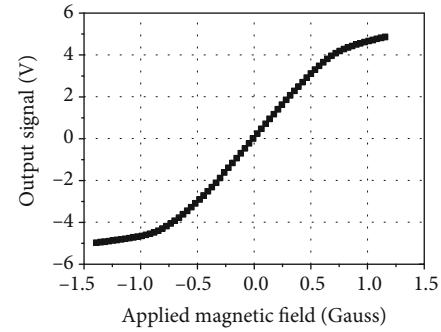

Figure 4: Output voltage of the magnetic sensor without feedback changes with the applied external magnetic field.

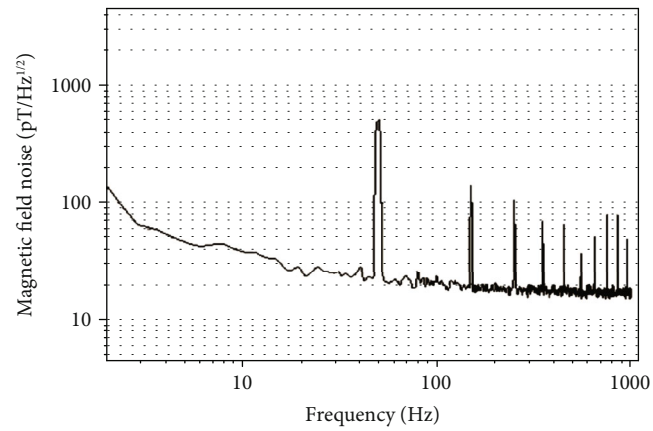

Figure 5: Magnetic field noise spectrum of the magnetic sensor measured in a permalloy shielding box.

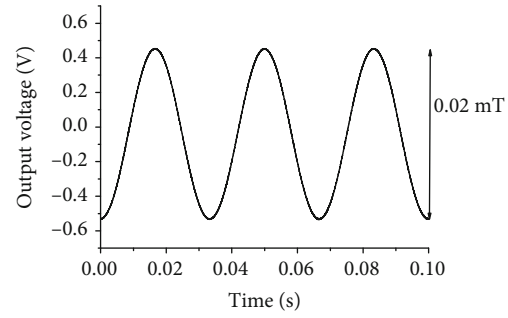

Figure 6: Output signal of the magnetic field sensor without feedback for the 30 Hz applied magnetic field with the amplitude of 0.2 Gauss (0.02 mT).

where A_1 is the signal amplitude of the fundamental frequency f; $A_2, A_3, \ldots$ are the amplitudes of the harmonics with the frequencies of $2f$, $3f$, …, which can be measured by a spectrum analyzer.

Figure 9 shows the experimental setup to measure the THD of the GMI sensor. The coil connected with the sine wave generator was used to produce the applied magnetic field. The harmonic distortion of the signal generated by the generator was below 5×10^{-4}. A spectrum analyzer was used to measure the THD of the output signals of the MI magnetic field sensor. To measure the small harmonic signals accurately, the influence of fundamental frequency signal must be reduced. A resistance trimmer was used to suppress the fundamental frequency signal of MI sensor output. By this method, the influence of the harmonics of the input signal could also be reduced.

In the measurement, the resistance of R1 was first adjusted to make the output of the MI magnetic field sensor be equal to the voltage of the sine wave generator; then, the resistance trimmer R2 was adjusted to cancel the fundamental signal of the sensor output. We estimated that the relative error of our measurement was about 10%.

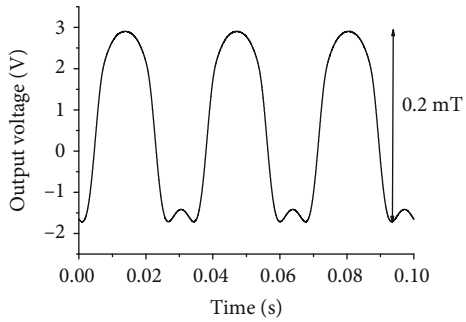

Figure 7: Output signal of the magnetic field sensor without feedback for the 30 Hz applied magnetic field with the amplitude of 2 Gauss (0.2 mT).

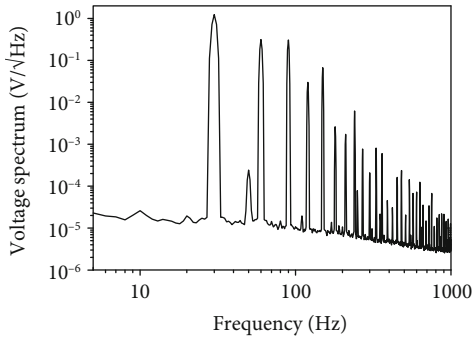

Figure 8: Output voltage spectrum of the MI magnetic field sensor without feedback for the 30 Hz applied magnetic field with the amplitude of 2 Gauss.

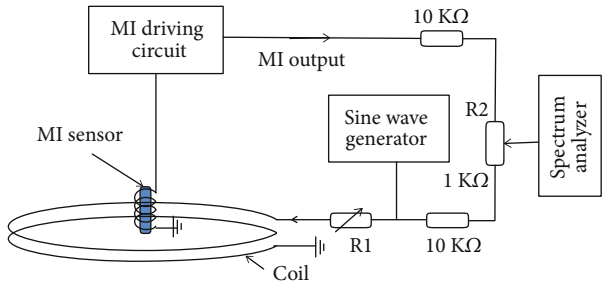

Figure 9: Setup of nonlinearity measurement.

Figure 10 shows the THD of the sensor without feedback for the 30 Hz applied magnetic field. It increased with the amplitude of the applied magnetic field.

3. MI Magnetic Sensor with Feedback

Magnetic feedback method is a good way to increase the linearity of magnetic sensor [18]. Figure 11 shows the block diagram of the MI magnetic field sensor with feedback. After the demodulation and an amplifier, an integrator was used. A feedback current produced by the output of the integrator and the feedback resistor R_F was sent to the coil wrapped around the amorphous wire. The magnetic field produced by the feedback current automatically compensated the

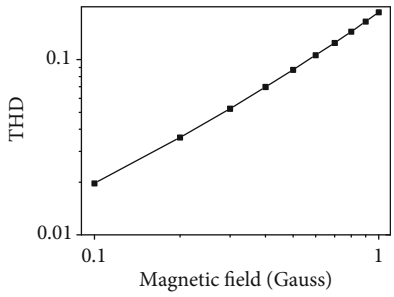

Figure 10: THD of MI magnetic field sensor without feedback for the 30 Hz applied magnetic field with different amplitudes.

applied magnetic field. Thus, the operation point of the MI magnetic field sensor was fixed. By this way, the dynamic range and the linearity of the system can be dramatically improved. When the switch SW was off, the driving circuit operated in amplifier mode. The output voltage V of the amplifier responded to the magnetic field. When the switch SW was on, the driving circuit operated in feedback mode. A feedback current V_{out}/R_F was produced, and the magnetic field produced by the feedback current was equal to the applied magnetic field. Thus, the output voltage V_{out} was proportional to the applied magnetic field.

Figure 12 shows the output voltage of the MI magnetic field sensor with feedback changing with the applied external magnetic field. We can see that the linearity was very good for the applied external magnetic field between -10 Gauss and +10 Gauss. Compared with Figure 4, the dynamic range and the linearity were much improved.

With the feedback, the magnetic field resolution of the MI magnetic field sensor was similar with that of without feedback. To check the magnetic field resolution, a small 30 Hz magnetic field with the amplitude of about 2 nT was applied. Figure 13 shows the output signal of the MI magnetic sensor. To remove the 50 Hz inference, the observation bandwidth was about 40 Hz.

Figure 14 shows the output signal of the MI magnetic field sensor with feedback when the amplitude of the 30 Hz applied magnetic field was 2 Gauss (0.2 mT); and Figure 15 shows the output signal when the amplitude was 20 Gauss (2 mT). The distortions of the signals were very small even for a strong magnetic field of 2 mT. The feedback method was effective to improve the linearity of the magnetic field sensor.

Figure 16 shows the spectrum of the output signal of the MI magnetic field sensor with feedback for the 30 Hz applied magnetic field with the amplitude of 2 Gauss. Compared with the spectrum of the output signal without feedback shown in Figure 8, the amplitudes of the 30 Hz harmonics were much small.

Using the setup shown in Figure 9, we also measured the THD of the MI magnetic sensor with feedback for the 30 Hz applied magnetic field with different amplitudes. Figure 17 shows the results. For the amplitude of 1 Gauss, the THD of the signal with feedback was about 1.4×10^{-4}, which was about 1% of the THD value without feedback. The linearity can be much improved using the feedback method.

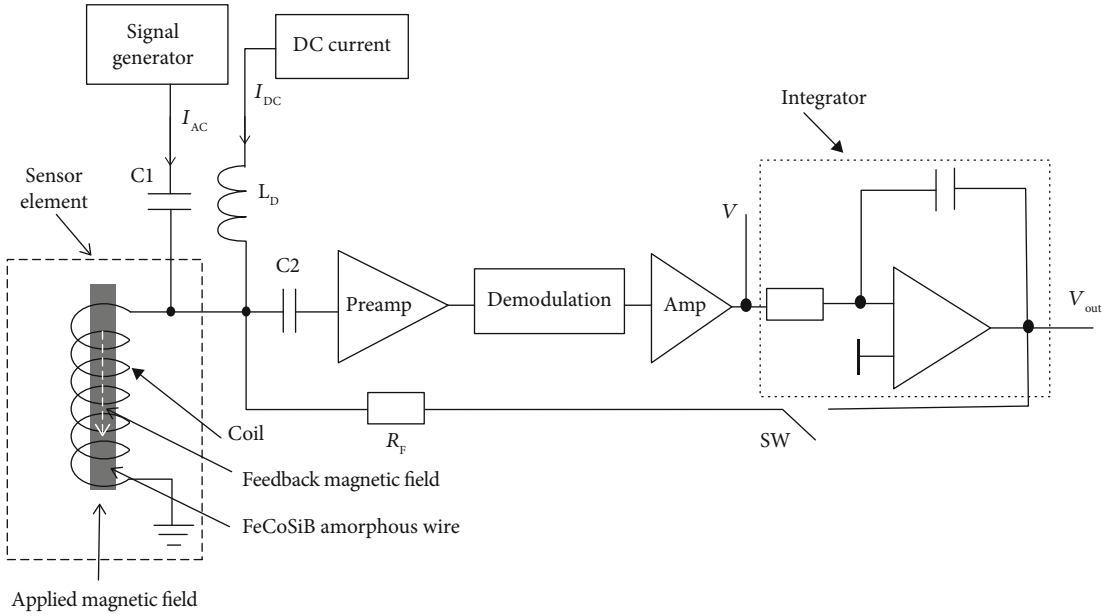

Figure 11: Block diagram of the MI magnetic field sensor and the driving circuit with feedback.

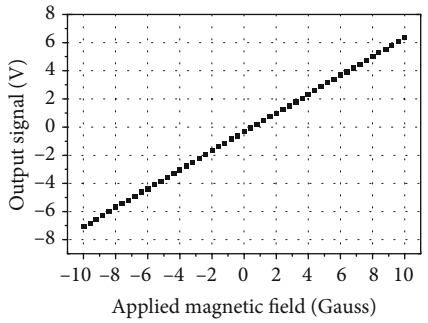

Figure 12: Output voltage of the magnetic sensor with feedback changes with the applied external magnetic field.

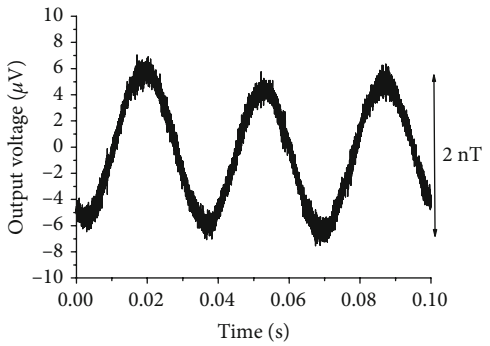

Figure 13: Output signal of the magnetic field sensor for the 30 Hz applied magnetic field with the amplitude of 2 nT.

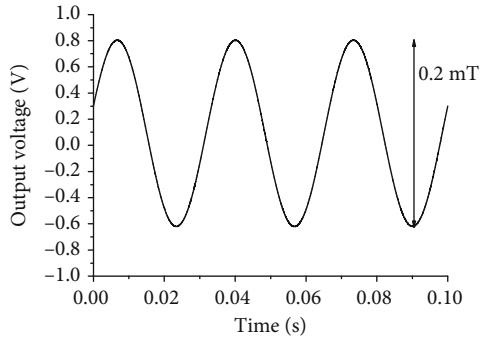

Figure 14: Output signal of the magnetic field sensor for the 30 Hz applied magnetic field with the amplitude of 2 Gauss (0.2 mT).

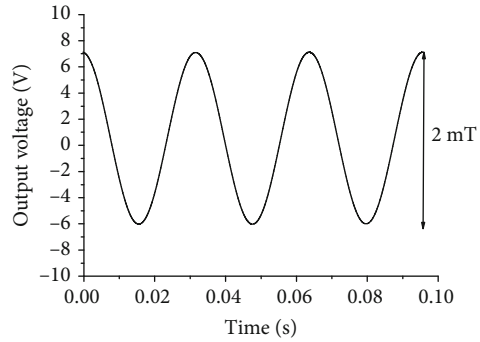

Figure 15: Output signal of the magnetic field sensor for the 30 Hz applied magnetic field with the amplitude of 20 Gauss (2 mT).

4. Eddy Current Testing Using MI Magnetic Sensor with Feedback

Figure 18 shows the block diagram of the ECT system using the MI magnetic field sensor with feedback. The excitation coil was 10 turns with the diameter of approximately 1 mm and was also wrapped around the FeCoSiB amorphous wire. The sine wave output of the lock-in amplifier was sent to the excitation coil to produce the excitation magnetic field. The excitation frequency was 20 kHz and the current amplitude was 20 mA. The amplitude of the magnetic field in the centre

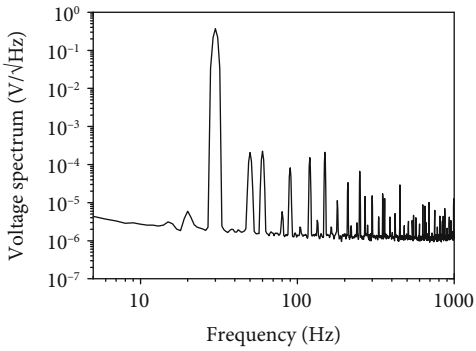

Figure 16: Output voltage spectrum of the MI magnetic field sensor with feedback for the 30 Hz applied magnetic field with the amplitude of 2 Gauss.

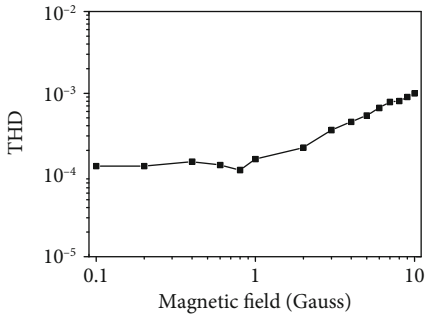

Figure 17: THD of MI magnetic field sensor with feedback for the 30 Hz applied magnetic field with different amplitudes.

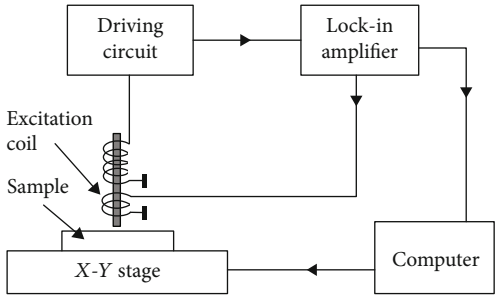

Figure 18: Block diagram of the ECT system with amorphous wire magnetic sensor.

of the excitation coil was about 2 Gauss. The MI magnetic field sensor was used to measure the magnetic field produced by the eddy current in the sample. The sample was put on an X-Y stage for the scanning. Figure 19 shows the photo of the setup.

Figure 20 shows the Ti-6L-4V titanium alloy sample fabricated by 3D laser printing. The size of the sample was 50 $\times$ 50 $\times$ 10 mm. There were two surface flaws extending from the edges of the sample. The length of flaw a was about 13 mm with the depth of about 1.5 mm, and the width of flaw a was from 0.2 mm to about 10 μm. The length of flaw b was about 15 mm with the depth of about 5 mm, and the width of flaw b was from 0.3 mm to about 10 μm.

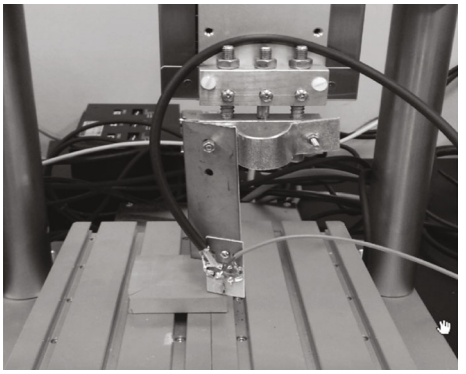

Figure 19: Photo of the ECT setup.

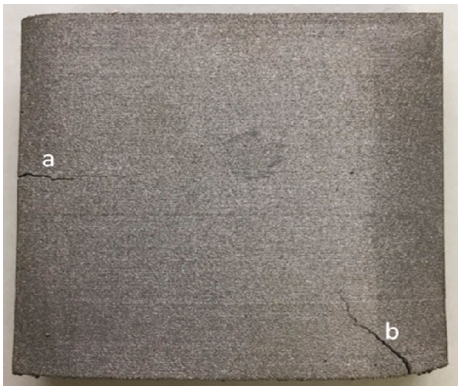

Figure 20: Photo of titanium alloy sample fabricated by a 3D laser printer.

Figure 21 shows the ECT result using the amorphous wire magnetic sensor. The scanning area was 45 mm $\times$ 45 mm and scanning step was 0.2 mm. The amplitude output signal of the lock-in amplifier was used to plot the 2D graph. The defects were displayed clearly.

We also evaluated the defect in the steel plate using the ECT system. The thickness of the steel plate was 3 mm. In the steel plate, there was a small hole defect with the size of about 1.5 mm and the depth of about 2 mm. The steel plate produced a strong magnetic field of about 5 Gauss. The MI magnetic sensor with feedback could operate well during scanning. An excitation coil with the diameter of about 3 mm was used.

The determination of the excitation frequency is an important factor in ECT, because the penetration of eddy current is limited by the skin effect. The skin depth is defined by $\delta = (\pi f \mu \sigma)^{-1/2}$, where δ is the skin depth, μ is the magnetic permeability, σ is the electrical conductivity, and f is the frequency. For the steel plate, the conductivity σ is about 2 $\times$ 106 S/m, the relative permeability is about 100, and the penetration depth is about 2.7 mm at the frequency of 170 Hz.

To detect deep defect in the steel plate, a lower excitation frequency of 170 Hz was used. The amplitude of the excitation current was about 20 mA. Figure 22 shows the

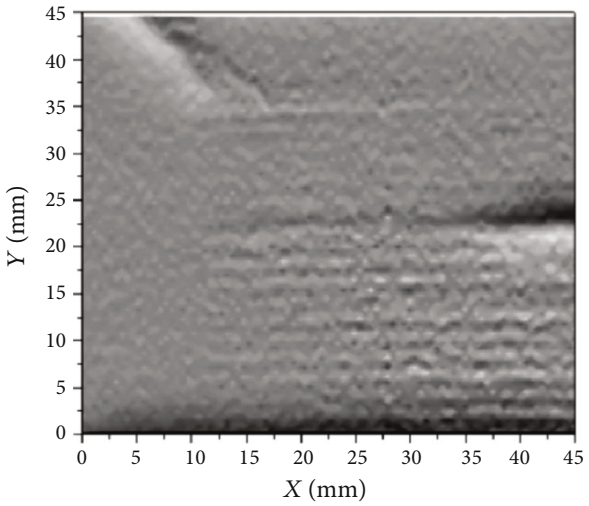

Figure 21: Scanning results by the ECT system with amorphous wire magnetic sensor.

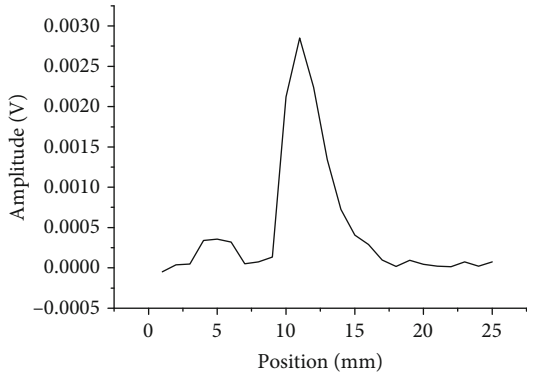

Figure 22: One scanning signal of a defect in the steel plate.

defect signal of one scanning, and Figure 23 shows the 2D scanning results.

5. Conclusion

A feedback method was developed for the MI magnetic field sensor. Using the feedback method, the dynamic range of the MI sensor was improved from ±0.7 Gauss to ±10 Gauss, and the linearity of the magnetic sensing system was also improved. The THD of the output signal with the feedback was about 1% of the THD without feedback.

If the MI sensor is used in an industrial environment, the amplitude of the 50 Hz line interference can be up to 1 μT. For the MI sensor without feedback, the signal distortion caused by the nonlinearity is about 10 nT, which is big enough to influence the accuracy of the detection. For the MI sensor with feedback, the signal distortion is about 100 pT, which is close to the magnetic field noise of the GMI sensor and has less influence to the accuracy of the detection. Therefore, for the applications in the industrial environment, the MI sensor with feedback is necessary.

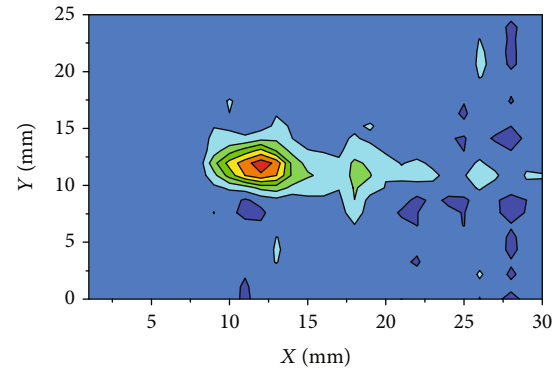

Figure 23: 2D scanning result of the defect in the steel plate.

We constructed the ECT system using the MI magnetic field sensor with feedback. Because of its big dynamic range, it can be used to evaluate defects in the steel plate. We will find more industrial applications for our magnetic field sensing system.

Data Availability

The ASCII data used to support the findings of this study were supplied by Dongfeng He under license and so cannot be made freely available. Requests for access to these data should be made to Dongfeng He (he.dongfeng@nims.go.jp).

Conflicts of Interest

The author declares that he has no conflicts of interest.

References

[1] L. V. Panina, K. Mohri, K. Bushida, and M. Noda, "Giant magneto-impedance and magneto-inductive effects in amorphous alloys (invited)," *Journal of Applied Physics*, vol. 76, no. 10, pp. 6198–6203, 1994.

[2] L. G. C. Melo, D. Ménard, A. Yelon, L. Ding, S. Saez, and C. Dolabdjian, "Optimization of the magnetic noise and sensitivity of giant magnetoimpedance sensors," *Journal of Applied Physics*, vol. 103, no. 3, article 033903, 2008.

[3] K. Mohri, F. B. Humphrey, L. V. Panina et al., "Advances of amorphous wire magnetics over 27 years," *Physica Status Solidi*, vol. 206, no. 4, pp. 601–607, 2009.

[4] S. Dwevedi, G. Sreenivasulu, and G. Markandeyulu, "Contact and non-contact magnetoimpedance in amorphous and nanocrystalline $Fe_{73.5}Si_{13.5}B_8CuV_3Al$ ribbons," *Journal of Magnetism and Magnetic Materials*, vol. 322, no. 3, pp. 311–314, 2010.

[5] K. Mohri, T. Uchiyama, L. P. Shen, C. M. Cai, and L. V. Panina, "Amorphous wire and CMOS IC-based sensitive micro-magnetic sensors (MI sensor and SI sensor) for intelligent measurements and controls," *Journal of Magnetism and Magnetic Materials*, vol. 249, no. 1-2, pp. 351–356, 2002.

[6] M. Tibu and H. Chiriac, "Amorphous wires-based magneto-inductive sensor for nondestructive control," *Journal of Magnetism and Magnetic Materials*, vol. 320, no. 20, pp. e939–e943, 2008.

[7] T. Uchiyama, S. Nakayama, K. Mohri, and K. Bushida, "Biomagnetic field detection using very high sensitivity magnetoimpedance sensors for medical applications," *Physica Status Solidi A: Applications and Materials Science*, vol. 206, no. 4, pp. 639–643, 2009.

[8] D. F. He, Z. Wang, M. Kusano, S. Kishimoto, and M. Watanabe, "Evaluation of 3D-Printed titanium alloy using eddy current testing with high-sensitivity magnetic sensor," *NDT & E International*, vol. 102, pp. 90–95, 2019.

[9] T. Uchiyama and J. J. Ma, "Design and demonstration of novel magnetoencephalogram detectors," *IEEE Transactions on Magnetics*, vol. 55, no. 7, pp. 1–8, 2019.

[10] K. N. Choi, "Metal detection sensor utilizing magneto-impedance magnetometer," *Journal of Sensors*, vol. 2018, Article ID 3675090, 9 pages, 2018.

[11] D. F. He, M. Daibo, and M. Yoshizawa, "Mobile HTS rf SQUID magnetometer," *IEEE Transactions on Applied Superconductivity*, vol. 13, no. 2, pp. 200–202, 2003.

[12] D. F. He, M. Tachiki, and H. Itozaki, "Highly sensitive anisotropic magnetoresistance magnetometer for Eddy-current nondestructive evaluation," *The Review of Scientific Instruments*, vol. 80, no. 3, article 036102, 2009.

[13] D. Drung, "High-T_c and low-T_c dc SQUID electronics," *Superconductor Science & Technology*, vol. 16, no. 12, pp. 1320–1336, 2003.

[14] D. F. He and M. Shiwa, "A magnetic sensor with amorphous wire," *Sensors*, vol. 14, no. 6, pp. 10644–10649, 2014.

[15] D. G. Nichols, E. Dantsker, R. Kleiner, M. Mück, and J. Clarke, "Linearity of high-T_c dc superconducting quantum interference device operated in a flux-locked loop," *Journal of Applied Physics*, vol. 80, no. 10, pp. 6032–6038, 1996.

[16] J. Beyer, D. Drung, F. Ludwig, and T. Schurig, "Linearity of sensitive $YBa_2Cu_3O7_{-x}$ dc superconducting quantum interference device magnetometers," *Journal of Applied Physics*, vol. 86, no. 6, pp. 3382–3386, 1999.

[17] D. F. He, Y. Zhang, A. I. Braginski, Y. D. Dai, and S. Z. Wang, "The nonlinearity of the high-Tc rf SQUID system," *Physica C: Superconductivity*, vol. 341-348, Part 4, pp. 2695-2696, 2000.

[18] D. F. He and M. Shiwa, "High sensitive magnetic sensor with amorphous wire," in *2015 9th International Conference on Sensing Technology (ICST)*, pp. 8–10, Auckland, New Zealand, December 2015.

Hindawi
Journal of Sensors
Volume 2019, Article ID 6078591, 12 pages
https://doi.org/10.1155/2019/6078591

Research Article

Analysis on Precipitable Water Vapor over the Tibetan Plateau Using FengYun-3A Medium Resolution Spectral Imager Products

Shaoqi Gong,[1,2,3] **Daniel F. T. Hagan**,[1] **and Cunjie Zhang**[2,4]

[1]*School of Remote Sensing and Geomatics Engineering, Nanjing University of Information Science & Technology (NUIST), Nanjing 210044, China*
[2]*National Climate Center, China Meteorological Administration, Beijing 100081, China*
[3]*NUIST-UoR International Research Institute, Nanjing 210044, China*
[4]*Key laboratory for Cloud Physics of China Meteorological Administration, Beijing 100081, China*

Correspondence should be addressed to Cunjie Zhang; 693246609@qq.com

Received 30 March 2019; Accepted 26 August 2019; Published 28 November 2019

Guest Editor: Dongfeng He

The Tibetan Plateau is the largest and highest plateau in the world, and its complex terrain affects the distribution of precipitable water vapor (PWV) in the atmosphere, which plays an important role in the weather and climate of East Asia. In this paper, the characteristics of PWV over the Tibetan Plateau are studied using the FengYun-3A Medium Resolution Spectral Imager (MERSI) water vapor products, which are retrieved from the MERSI raw images of Chinese second-generation polar orbit meteorological satellite. Firstly, the accuracy of the MERSI 5-minute water vapor product is validated using three referenced water vapor data from TERRA/MODIS, ground-based GPS, and AERONET sun photometer over the Tibetan Plateau. Then, the spatial distribution and seasonal variation of PWV over the plateau are analyzed, and the effects of topographic factors on PWV are discussed. The results indicate that the MERSI 5-minute water vapor product has a good accuracy over the Tibetan Plateau, which the mean absolute error of MERSI water vapor product is in the range of 28.91%-37.54%, the mean absolute error range between 1.87 and 2.76 millimeter (mm), and the mean bias is between -1.14 and 0.64 mm comparing three referenced data. The PWV content appears as a typical spatial pattern over the Tibetan Plateau where there is a decrease from east to west of the Tibetan Plateau with increasing elevation, with the highest values over the south of Tibet. A second pattern also appears over the eastern part of the Tibetan Plateau, where the PWV content in the Qaidam Basin and the south of Tarim Basin are also considerably high. The seasonal variation of PWV content over the Tibetan Plateau presents to be highest in summer, followed by autumn and spring, and lowest in winter. The PWV content changes periodically during the year, which fits with a quadratic polynomial over monthly scales. The topographical factors of the Tibetan Plateau were found to affect the water vapor, where the altitude and latitude are negatively correlated with water vapor, while the slope and longitude show a positive correlation with water vapor; however, the aspect does not appear to have any significant influence on water vapor.

1. Introduction

The Tibetan Plateau is the highest and largest plateau in the world and is surrounded by the highest mountains on Earth. It is called the roof of the world, as well as the third pole of the earth [1]. The elevation in the most areas is 6000-7000 m and the average altitude is above 4000 m. The distances are 2800 km in the east-west direction and 300-1500 km from north to south, with a total area of about 2.4 million km^2, accounting for about 1/4 of land area of China [2]. Large-scale complex terrain on the plateau can block, divert, and direct the atmospheric circulation. It also influences the solar radiation and the energy balance of the earth and atmosphere system [3]. Hence, the Tibetan Plateau plays an important role within the weather and climate of East Asia, and even globally [4]. Due to the thermodynamic forcing of the plateau, the precipitable water vapor (PWV) content over the Tibetan Plateau possesses significant temporal and spatial variability [5]. Since PWV is a key atmospheric constituent despite the low proportion in the atmosphere, it is a

necessary factor to generate cloud and precipitation, and it can affect the local water circulation process, heat up the whole climate system, and produce global greenhouse effects [6]. The research on the water vapor over Tibetan Plateau is useful to understand the water cycle process in the surrounding areas, the ecological environmental changes, the drought and flood disasters, and several weather and climatic phenomena.

As for the PWV measurement methods, the ground-based GPS [7], Sun photometer [8], microwave radiometer [9], and radiosonde [10] can accurately measure the atmospheric water vapor. Since the number of observation station is limited, and its distribution is uneven, the instrument measurements on ground cannot be applied to properly study the of PWV spatial distribution characteristics. The NCEP/NCAR reanalysis data and NVAP dataset can provide global water vapor data [11], but the spatial resolution is too low. With the development of remote sensing technology, there has been some satellite remote sensing water vapor products with high temporal and spatial resolution, such as the water vapor product of TERRA/MODIS which was developed by Gao and Kaufman [12, 13] with the MODIS original images in the near-infrared channels, that of FY-3A/MERSI which was developed by the National Satellite Meteorological Center of China from raw data in the near-infrared channels of the Medium Spectral Resolution Imager (MERSI) onboard the FY-3A satellite. At present, more researchers have employed the use of MODIS water vapor products [13–16] while less make use of the MERSI water vapor products in the research. So this paper will firstly validate the MERSI water vapor products over the Tibetan Plateau, then analyze the temporal and spatial distribution characteristics of water vapor over the Plateau, and finally discuss the influence of the Plateau topography on water vapor.

2. Data and Methods

2.1. FY-3A/MERSI Water Vapor Products. FY-3A was the first spacecraft among the second generation of Chinese polar orbit meteorological series satellites, which was launched on May 27, 2008 with a 836 km altitude, near-sun synchronous orbit, and the passing time for 10:30 A.M at an equatorial descending node. The Medium Resolution Spectral Imager (MERSI) is a payload onboard FY-3A, containing 20 channels with the spectral coverage from visible, near-infrared to thermal infrared band, and MERSI has two nadir spatial resolutions with 250 m for channel 1-5 and 1000 m for channel 6-20, their spectral specifications can be seen in Reference [17]. MERSI can provide daily observations for the global scientific studies about the atmosphere, ocean, and land. The National Satellite Meteorological Center of China has developed the atmospheric PWV products using the MERSI raw data in the near-infrared channels, which include 5-minute, global daily, 10-day, and monthly water vapor products. And the MERSI daily, 10-day and monthly water vapor products with global coverage and 5 km spatial resolution are aggregated by the 5-minute one after some preprocessing procedures, such as the projection transformation and image mosaicking.

The retrieval principle of the MERSI water vapor product is the differential absorption method [18]. Because the strong absorption of water vapor occurs in the three near-infrared channels (centered at 0.905, 0.940, and 0.980 μm) and the weak absorption appears in their nearby atmospheric window channels (centered at 0.865 and 1.030 μm), the channel ratio from the absorption and window channel calculated by Equation (1) or (2) can reflect the absorption properties of water vapor.

$$\frac{\rho^*_{\mathrm{PWV}}}{\rho^*_0} = \left(\frac{\rho_{\mathrm{PWV}}}{\rho_0}\right)\rho_0, \tag{1}$$

$$\frac{\rho^*_{\mathrm{PWV}}}{(k_{01}\rho^*_{01} + k_{02}\rho^*_{02})} = \left[\frac{\rho_{\mathrm{PWV}}}{(k_{01}\rho_{01} + k_{02}\rho_{02})}\right]T_{\mathrm{PWV}}, \tag{2}$$

where ρ^* and ρ are the reflectance at the top of the atmosphere and surface, respectively; the subscript PWV and 0 are the absorption and window channels, respectively; 01 and 02 are the two adjacent window channels, while k_{01} and k_{02} are the scale factors between the absorption and window wavelength λ. It can be calculated by Equations (3) and (4):

$$k_{01} = \frac{(\lambda_{\mathrm{PWV}} - \lambda_{01})}{(\lambda_{02} - \lambda_{01})}, \tag{3}$$

$$k_{02} = \frac{(\lambda_{02} - \lambda_{\mathrm{PWV}})}{\lambda_{02} - \lambda_{01}}. \tag{4}$$

When the surface is covered by only one natural feature and the wavelengths of the absorption and window channels are very close, ρ_{PWV} is approximately equal to ρ_0; thus, Equation (1) can be rewritten as shown in Equation (5).

$$\frac{\rho^*_{\mathrm{PWV}}}{\rho^*_0} = T_{\mathrm{PWV}}. \tag{5}$$

Assuming that the surface reflectance varies linearly with wavelength, the reflectance in the absorption channel can be expressed by that in two window channels, that is $\rho_{\mathrm{PWV}} = k_{01}\rho_{01} + k_{02}\rho_{02}$ [2, 13]; hence, Equation (2) can be also be rewritten as shown in Equation (6).

$$\frac{\rho^*_{\mathrm{PWV}}}{(k_{01}\rho^*_{01} + k_{02}\rho^*_{02})} = T_{\mathrm{PWV}}. \tag{6}$$

Therefore, the atmospheric water vapor transmittance in the three absorption channels can be derived by the channel ratio, respectively, and the water vapor content of each channel is extrapolated according to the lookup table of water vapor and transmittance. Since the sensitivity in the different absorption channels is distinct for the PWV content, the sensitivity η is defined by taking the derivative of transmittance

Table 1: Date of MERSI 5-minute water vapor product and three referenced water vapor data.

Season	Date
Winter	January to February 2010; December 1, 2010 to January 12, 2011; December 2011; January 2012; January 20 to February 28 2013
Spring	March and April 2012; April and May 2010; April 2013
Summer	July 1 to August 10, 2012; June and July 2010; July 2013; June and August 2011
Autumn	October 2 to November 30, 2009; October 2010 and 2013; September to November 2011

on PWV content, $\eta_i = \Delta\tau_i/\Delta\mathrm{PWV}_i$, here i is the number of absorption channel. Finally, the PWV content is calculated from that of three absorbing channels by the sensitivity weighted mean, $\mathrm{PWV} = \sum f_i \mathrm{PWV}_i$, where f_i is the weighting function of the i^{th} absorption channel which is defined as $f_i = \eta_i/(\eta_1 + \eta_2 + \eta_3)$. In order to utilize MERSI water vapor products in this research, the accuracy of MERSI water vapor 5-minute product is validated, respectively, with three synchronous referenced water vapor data retrieved from the measurements of the ground-based GPS, AERONET Sun photometer [19], and Terra/MODIS. The validated data cover four seasons including spring, summer, autumn, and winter and their dates are summarized in Table 1. Since the weather is not always sunny during these dates, the water vapor data from Sun photometer, MERSI, and MODIS are also not continuous. Furthermore, MERSI monthly water vapor products from February 2010 to September 2015 are applied to analyze the spatial and temporal variability of water vapor over the Tibetan Plateau. All the MERSI water vapor products are available in the FengYun satellite remote sensing data service network (http://satellite.cma.gov.cn/portalsite/default.aspx).

2.2. The Referenced Water Vapor Data

2.2.1. Water Vapor Data from the Ground-Based GPS. With the rapid development of the GPS meteorology since the 1980s, the PWV content retrieved from the measurements of the ground-based GPS has an accuracy with a root-mean-square of 1.0-2.1 mm in contrast with that from the microwave radiometer or radiosonde [20–23]. The atmospheric PWV content is able to be calculated accurately from GPS estimates of troposphere zenith path delay (ZPD) at the ground tracking stations. And the International GNSS Service (IGS) provides a long-term and continuous ZPD product for a 5-minute interval at the level of 4-6 mm corresponding to the PWV error less than 1 mm [24]. There is an available IGS station with elevation 3622 m in the Tibetan Plateau (Figure 1). Generally, the troposphere zenith path delay is sourced from two parts: a zenith hydrostatic delay (ZHD) and a zenith wet delay (ZWD). The ZHD can be expressed as a function of the geodetic height H, geodetic latitude φ, and atmospheric pressure P_s [25], and the ZWD can be calculated by subtracting ZHD from ZPD. Then, PWV is obtained by ZWD multiplying a constant of proportionality Π. The algorithm about PWV calculated from GPS measurements is cited by Lu et al. [26]. The ZPD and relative meteorological data are available on the website ftp://cddis.gsfc.nasa.gov/. And the dates of all GPS water vapor data are corresponding to those of MERSI water vapor 5-minute product and summarized in Table 1.

2.2.2. AERONET Water Vapor Data. The AERONET (Aerosol Robotic Network) project is established by NASA and PHOTONS (Photométrie pour le Traitement Opérationnel de Normalisation Satellitaire) for a federation of ground-based remote sensing aerosol networks [19], which provides a long-term, continuous, and readily accessible public domain dataset of aerosol and water vapor. The Sun photometer CE318 with 8 channels ranged from 340 to 1020 nm (made by the French company CIMEL Electronique) is the standard instrument in the AERONET and is applied to observe aerosol optical parameters and PWV content for a 15-minute interval. Since the level 2.0 data of AERONET has undergone cloud screening and quality control, the uncertainty of AERONET water vapor data is 12% [27]. In this study, the water vapor data from 16 AERONET stations in the Tibetan Plateau (Figure 1) are considered the reference to validate the MERSI 5-minute water vapor product. The level 2.0 data of AERONET are derived from the website (http://aeronet.gsfc.nasa.gov/). And the dates of all AERONET data are corresponding to those of MERSI 5-minute water vapor product and summarized in Table 1.

2.2.3. TERRA/MODIS Water Vapor Data. Since FY-3A/MERSI has many similar characteristics with TERRA/-MODIS, such as the passing time at equatorial descending node, the water vapor absorption channels, radiometric and spatial resolution, and their retrieval algorithm of water vapor also used the differential absorption method in the near-infrared channels, MODIS water vapor data are a good reference for validating the accuracy of MERSI water vapor product because the error of MODIS water vapor retrieved directly from the L1b images is ±13% [12]. MODIS water vapor products (MOD05) are downloaded from the website (http://reverb.echo.nasa.gov/). And the dates of all MODIS water vapor data are corresponding to those of MERSI water vapor 5-minute product and summarized in Table 1.

2.3. Data of STRM DEM. The Shuttle Radar Topography Mission (STRM) is an international project spearheaded by NAG and NASA. SRTM was comprised of two specially modified radar systems, the C-band Spaceborne Imaging Radar and the X-band Synthetic Aperture Radar, which were flown on board the Space Shuttle Endeavour during the 11-day STS-99 mission on February 11-22, 2000 [28]. SRTM obtained the most complete and high-resolution digital elevation models (DEM) for approximately 80% of the world's land surface area from 56° S to 60° N. The DEM data has a post spacing of 1 arc second (often quoted as 30-

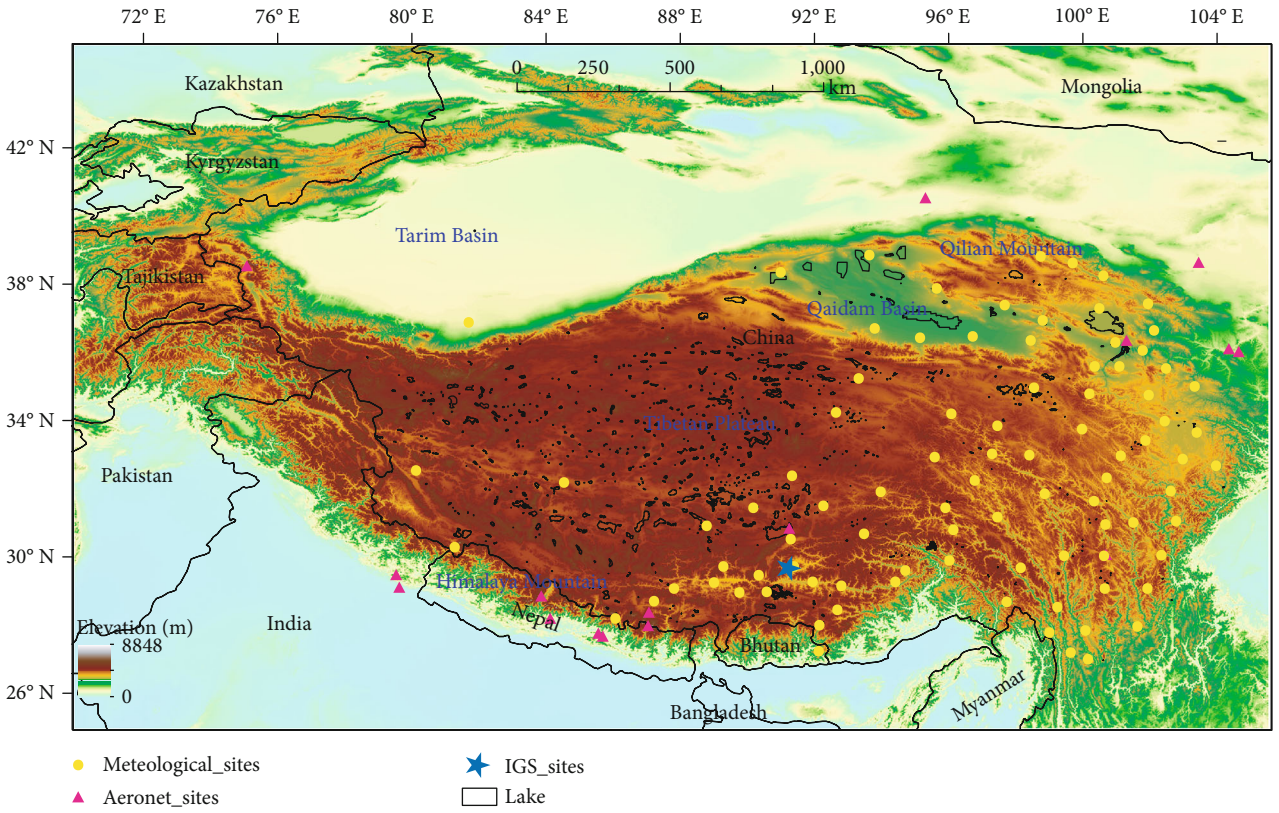

Figure 1: Distribution of referenced sites and the terrain in the Tibetan Plateau.

meter resolution) in the USA and a degraded 3 arc second (often quoted as 90-meter resolution) for the rest of the world with WGS84 geographic projection [29]. STRM DEM data for the Tibetan Plateau (Figure 1) were available on the CIAT-CSI SRTM website (http://srtm.csi.cgiar.org). For analyzing the influence of the terrain over the Tibetan Plateau on the distribution of water vapor, the slope and aspect was generated from DEM data by the Image Processing Software ENVI (Figure 2). All the data were resampled to 1 km resolution in order to match the MERSI water vapor products.

2.4. Preprocessing of MERSI Water Vapor Products. Since the MERSI 5-minute water vapor product includes the longitude and latitude data, the images of the product are firstly implemented geometrical correction using geographical coordinates with themselves. In order to compare MERSI water vapor product with the referenced water vapor data, the mean of the 3×3 neighborhood pixels corresponding to the centered location of referenced stations is calculated in the geometrically corrected MERSI PWV images. The matched time differences are controlled within 5 minutes, 15 minutes, and 30 minutes for ground-based GPS, Sun photometer, and Terra/MODIS, respectively.

As all the MERSI global monthly water vapor products are aggregated with a geographic coordinate system, here they only need to be registered. Taking MERSI monthly water vapor product in January, April, July, and October to stand for water vapor in winter, spring, summer, and autumn, respectively, all the monthly products in January, April, July, and October from February 2010 to September 2015 are averaged to represent the water vapor in the four seasons in order to analyze the spatiotemporal variability of water vapor over the Tibetan Plateau. After the averaged MERSI water vapor images are cut by the vector boundary map of Tibetan Plateau, the four seasonal distribution maps of water vapor are drawn. Furthermore, when every image of MERSI monthly water vapor product is overlapped on the vector polygon of the Tibetan Plateau, the average of all the pixels within the polygon is calculated and regarded as the monthly water vapor value over the plateau, and the time series chart of water vapor over the Tibetan Plateau is drawn. All the preprocess procedures are quickly implemented through the batch programming codes in the ENVI/IDL environment [30].

3. Results and Discussion

3.1. Accuracy Analysis of MERSI PWV Product over the Tibetan Plateau. Since MERSI global daily, 10-day, and monthly water vapor products are aggregated by the 5-minute one, and MERSI monthly water vapor products will be applied to analyze the spatiotemporal variation of water vapor over the Tibetan Plateau, the accuracy of MERSI 5-minute water vapor products is firstly evaluated by three sources of water vapor data retrieved from the measurements of TERRA/MODIS, the ground-based GPS, and AERONET sun photometer. Due to the measured errors of GPS or sun photometer and incomplete removal cloud of MODIS or

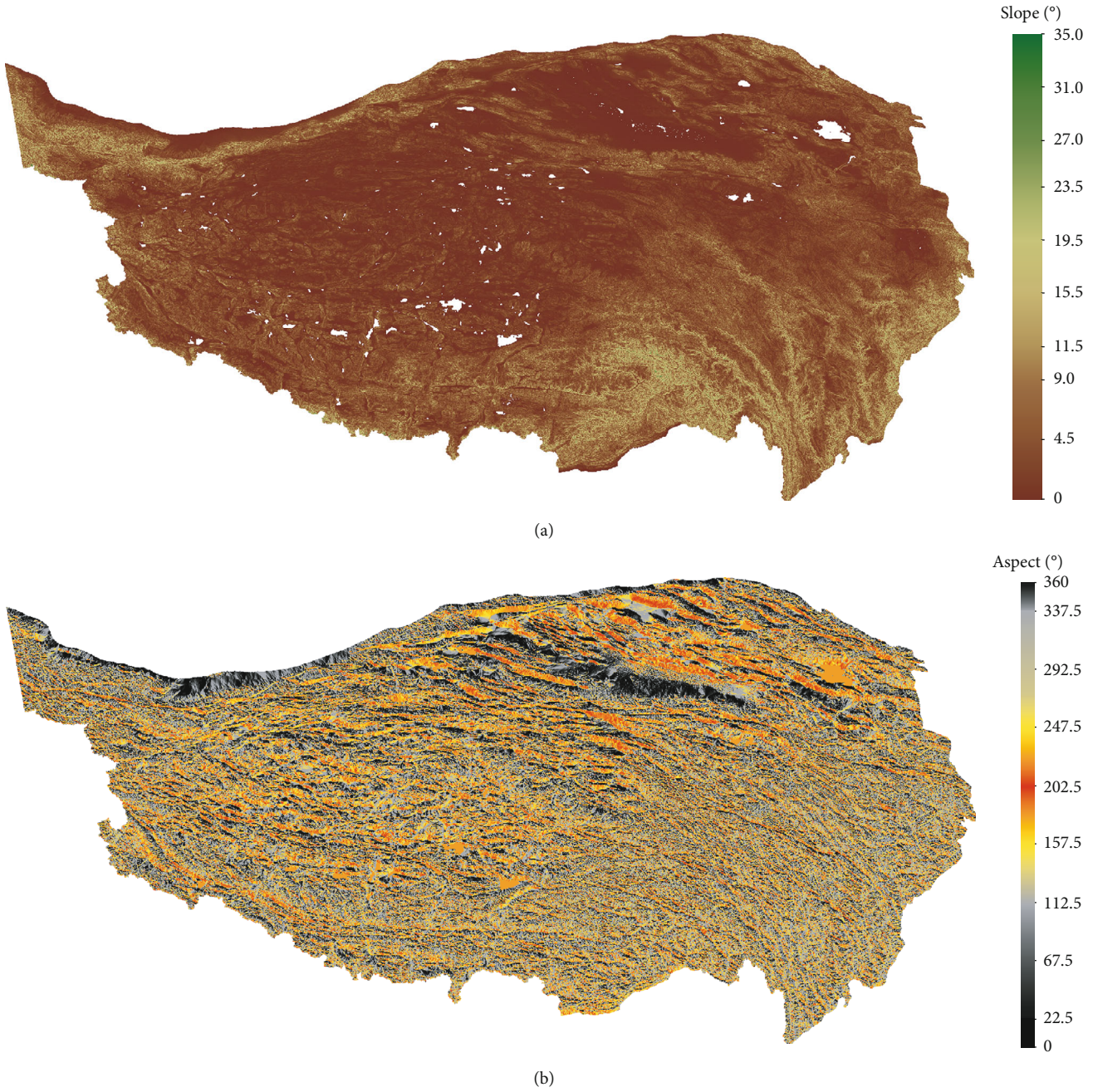

Figure 2: Slope and aspect of the Tibetan Plateau ((a) for slope and (b) for aspect).

MERSI raw images, there exists probably some outliers during the comparison. Therefore, the badly matched samples are removed automatically by a threshold value. When the outliers are eliminated from the matched samples, the scatter plots between the water vapor data of MERSI product and the reference are drawn, respectively, in Figure 3, and the evaluation indexes including Pearson's correlation coefficients (R), mean bias (MB), root mean square error (RMSE), and mean absolute percentage error (MAPE) are selected to evaluate the accuracy of MERSI water vapor products.

Seen from Figure 3, although the number of the matched water vapor samples between MERSI 5-minute product and the three referenced data are different, the correlation coefficients still are within a high range of 0.905 to 0.925, which are much higher than a threshold value 0.188 at a 99% confidence level for the least 205 degrees of freedom and indicate the most significant correlation between MERSI 5-minute product and the three referenced data. Furthermore, most of matched data points are distributed near the 1 : 1 line in the scatter plots. This shows that MERSI 5-minute water vapor product agrees well with the referenced water vapor datasets.

Figure 3(a) is the water vapor scatter plot between GPS and MERSI; the number of samples is the least with 207 since there is only one available IGS station in the Tibetan Plateau, but R is the highest with 0.925, and the values of MAPE and

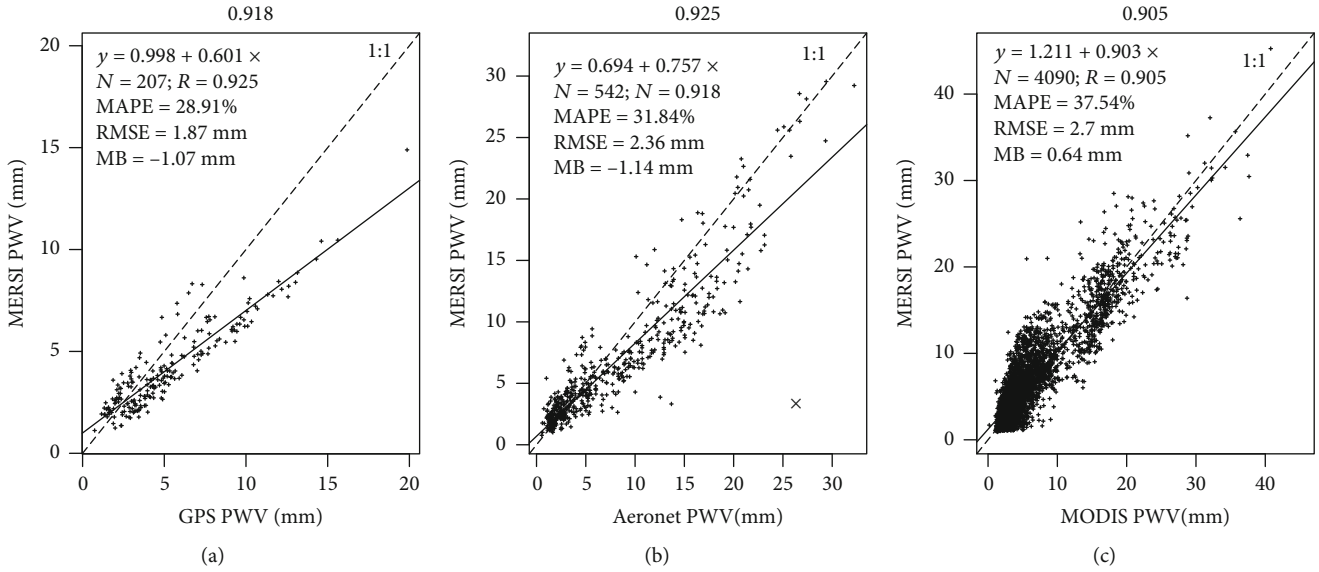

Figure 3: Comparison of water vapor values of MERSI with three referenced data ((a)-(c) represents the referenced data for GPS, AERONET, and MODIS, respectively).

RMSE are the smallest among the comparisons with three referenced data, that is, 28.91% and 1.87 mm, respectively. Since the passing time of FY-3A satellite over the Tibetan Plateau is very close to the GPS receiver receiving time, and their time difference is within 5 minutes, the variability of PWV content in situ is very small. The low errors show that MERSI 5-minute water vapor product has a good accuracy in the Tibetan Plateau. The MB is negative, at -1.07 mm, which shows that MERSI 5-minute water vapor product is relatively lower than water vapor of ground-based GPS. Since the number of the matched samples is few and the water vapor content is very low over the IGS station, a small bias between MERSI water vapor product and the water vapor of ground-based GPS will result in a large difference between 1 : 1 line and the regression line. Hence, the intercept of 0.998 and slope of 0.601 are a little far from 0 and 1, respectively. Figure 3(b) is water vapor scatter plot between AERONET sun photometer and MERSI, the number of samples is 542 and R is 0.918, indicating that MERSI water vapor product is in good agreement with AERONET data. The MAPE, RMSE, and MB between MERSI water vapor product and AERONET water vapor are 31.84%, 2.36 mm, and -1.14 mm, respectively, and the error values are in the middle among the comparisons with three reference data. The higher relative errors are due to two possible reasons except that the retrieval error of MERSI 5-minute water vapor product by itself. One is for the large uncertainty of AERONET water vapor data with 12%, and the other is the long time difference within 15 minute neighborhood during FY-3A satellite passing and Sun photometer observing at AERONET stations. The MB is also below 0, which shows that MERSI water vapor values are lower than the AERONET water vapor data. The intercept of 0.694 and slope of 0.757 are closer to 0 and 1, respectively; thus, the difference between the 1 : 1 line and the regression line is smaller than the comparison with the water vapor of ground-based GPS. Figure 3(c) is the water vapor scatter plot between MODIS and MERSI; the number of samples is the most with 4090 since the pixel values are derived from the two images by taking 91 meteorological stations in the Tibetan Plateau as the corresponding points. R is 0.905, showing MERSI water vapor values have a good correlation with those of MODIS. However, the errors here are the highest among the comparisons with three reference data, which the MAPE and RMSE are 37.54% and 2.76 mm, respectively. The errors between MERSI and MODIS water vapor products are also due to the high uncertainty of MODIS water vapor product with ±13% and the large overpass time difference of two satellites between FY-3A and TERRA about 30 minutes. Since most of matched water vapor samples are from the east of the Tibetan Plateau with relative higher water vapor values, and the number of samples is also the highest, the MB is very low with a positive value of 0.64 mm, indicating that the MERSI water vapor values are a little higher than those of MODIS over the Tibetan Plateau. The regression line here is the closest to the 1 : 1 line and the slope of 0.903 is also approaching 1 despite the intercept of 1.211 being far from 0. Consequently, the MAPE of MERSI water vapor product is in the range of 28.91%-37.54%, the RMSE ranges between 1.87 and 2.76 mm, and the MB between -1.14 and 0.64 mm during the comparisons with the three referenced data, and MERSI water vapor product has the best agreement with GPS water vapor data, the second with AERONET water vapor data, then with MODIS water vapor product, which shows that MERSI water vapor product has good accuracy over the Tibetan Plateau.

3.2. Temporal and Spatial Analysis of Water Vapor in the Tibetan Plateau. Figure 4 shows the four seasonal distribution maps of water vapor over the Tibetan Plateau, which are drawn with the mean of MERSI monthly water vapor products from 2010 to 2015, where (a)-(d) represent winter, spring, summer, and autumn, respectively. Known from

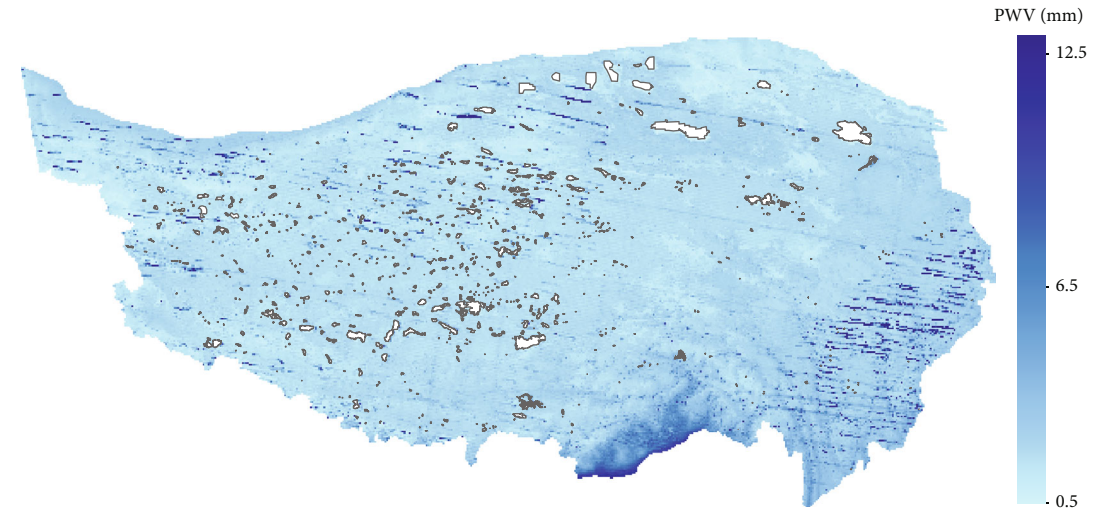

(a)

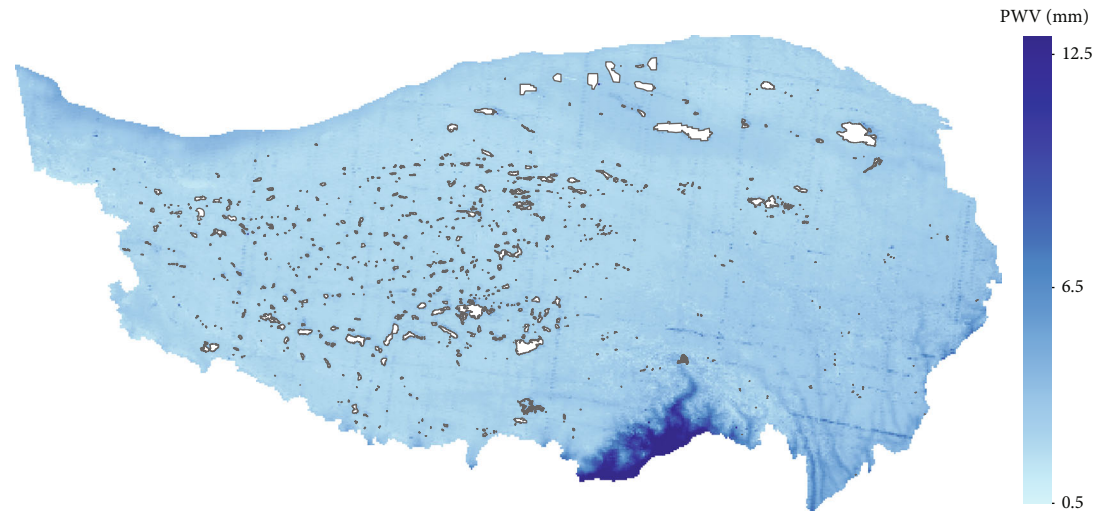

(b)

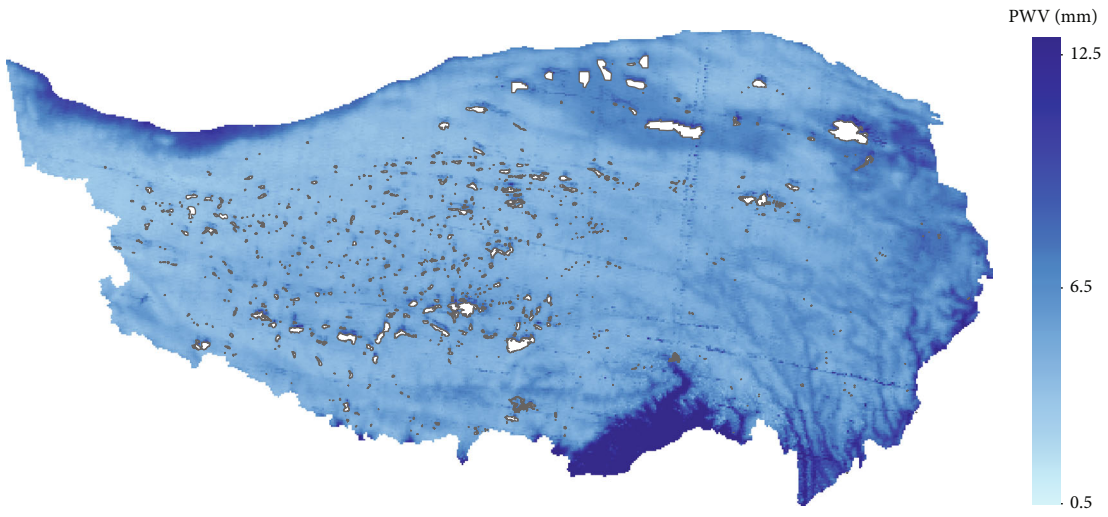

(c)

Figure 4: Continued.

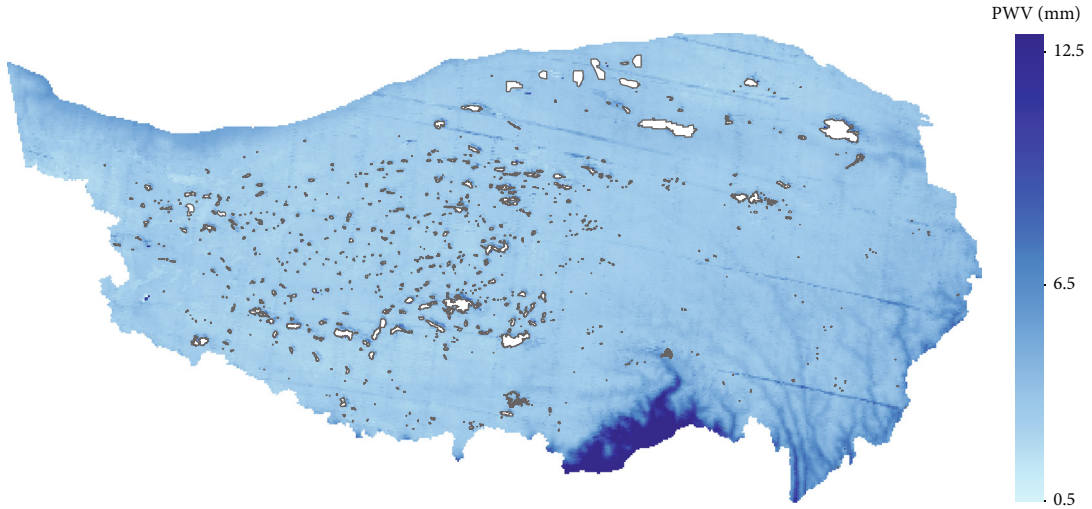

(d)

Figure 4: Seasonal distribution map of atmospheric water vapor over the Tibetan Plateau ((a)-(d) stands for winter, spring, summer, and autumn).

Figure 4, the spatial distribution of water vapor over the Tibetan Plateau displays the same pattern in the different seasons. There is the highest water vapor content for 12.50 mm in southern Tibet (called "Arunachal Pradesh" by India), where the elevation is low, appears to have both tropical and subtropical monsoon climates, and is affected by the Indian Ocean southwest monsoon, so there is the abundant moisture and heat due to enough rainfall and sunshine; therefore, it is warm and humid all year round [4, 5]. The PWV content is higher for 11.93 mm in the east of the Tibetan Plateau and it gradually decreases from east to west. It is also found to be high for 6.55 mm in the northern part of the Qaidam Basin with relatively low elevation. Although the PWV content in the west of Tibetan Plateau is the lowest with 0.50 mm, that in the northwest of Tibetan Plateau is relatively high with 9.47 mm, which lies in the southern margin of the Tarim Basin with the lower elevation. The spatial distribution of water vapor over the Tibetan Plateau is mainly related to elevation. The higher the elevation is, the shorter the column of atmospheric water vapor is. Research shows that 70-75% of the PWV content is located in the atmospheric layer from surface to 700 hPa in the low elevation area, while the PWV content is close to 0 in the surface -700 hPa layer in the areas above 3000 m where the surface atmospheric pressure is less than 700 hPa. Over the plateau, the 700-400hPa layer contains 80-90% of the water vapor and the 400-200 hPa layer contains 10-20% [10]. As the geopotential height increases, the water vapor content in the atmospheric column will reduce, so the integrated water vapor content is low in the areas with high elevation.

In order to analyze the seasonal distribution of water vapor over the Tibetan Plateau, the lake areas of the different sizes in the Tibetan Plateau have been masked. The water vapor over the Tibetan Plateau displays the distinct seasonal characteristics. The PWV content in winter is the lowest at 0.57-6.60 mm over the whole plateau. Spring and autumn is the transitional season between winter and summer, and the PWV content in the spring is the second lowest, with 1.20-6.80 mm. That in summer is the highest and it is 2.40-12.50 mm while that in autumn is the second highest for 1.55-10.00 mm. The seasonal variability of water vapor over the Tibetan Plateau is mainly due to the influence of the Asian monsoon circulation on water vapor transportation [31]. In winter, less water vapor is transported into the Tibetan Plateau and it is very dry since the influence of westerlies is weak, the current is blocked by the western terrain of Pamir Plateau, and water vapor is reduced from the northern Arabian Sea. In addition, the air temperature is also low in the Tibetan Plateau, the land surface is covered with much snow and ice, and the surface evaporation gets less. The transportation of water vapor in the plateau is enhanced gradually during spring. The water vapor from the Yarlung Zangbo Grand Canyon and the Tarim Basin, even from the Pamirs moves into the Tibetan Plateau region and the PWV content increases gradually. With the summer monsoon prevailing in Asia, water vapor from the South China Sea is transported westward and merges with water vapor from the Arabian Sea and the Bay of Bengal; hence, the Tibetan Plateau becomes a transfer station of water vapor over the continent, then the water vapor is transported continually to the east and north of China. Furthermore, since the plateau in summer is a main heat source where the thunderstorm and convection takes place frequently and atmospheric water vapor is majorly transported in the vertical. The snow is evaporated fast in mountains and the plant transpiration is increased, indicating the flood season with more rains in summer, these reasons will result in increasing the water vapor content over Tibetan Plateau. In autumn, the transportation of water vapor from the Arabian Sea to the Tibetan Plateau decreases and the PWV content in the plateau gets less [31].

In order to discover further the interannual variability of water vapor over the Tibetan Plateau, the time series chart of the monthly average water vapor content over the whole

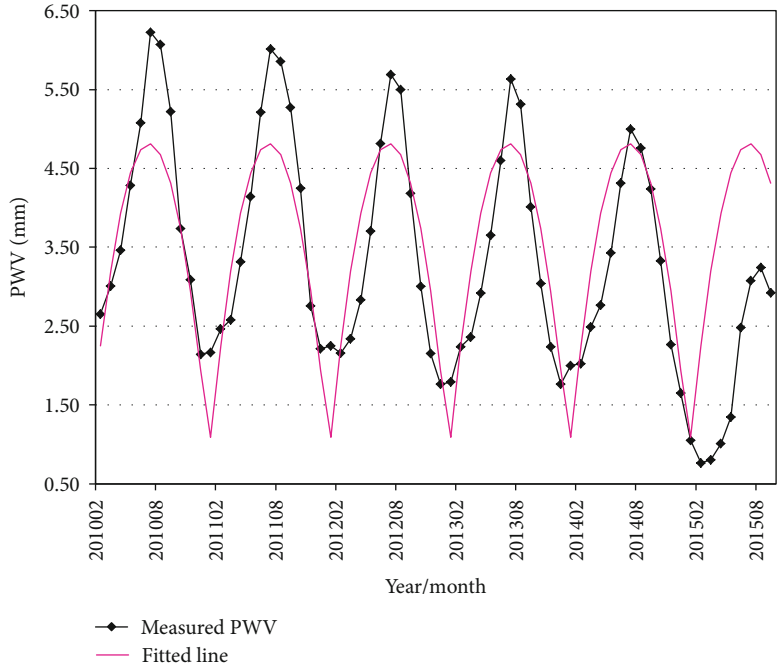

Figure 5: Time series chart of average water vapor content in the Tibetan Plateau.

plateau was made based on MERSI monthly water vapor product (Figure 5). Known from Figure 5, the water vapor over the Tibetan Plateau shows an annual periodic variation; the water vapor content is the lowest about 2.00 mm in December, and then increases monthly till it peaks with 6.00 mm in July and then decreases gradually. The relationship of annual water vapor content with month tends to a quadratic polynomial law. In this study, the average water vapor content over the Tibetan Plateau during February 2010 to December 2014 is fitted to a quadratic polynomial function, and the regression model is obtained as $\mathrm{PWV} = -0.2951 + 1.4916\,\mathrm{t} - 0.1088\,t^2$, where t is month, the number of samples for the model is 59, the coefficient of determination R^2 is 0.734, and the RMSE is 0.695 mm. The model reaches 99% significant level checked with F -test method. The values of statistical parameters R^2 and RMSE show that the fitted model has a good predicted accuracy. When the fitted regression line is added in the chart, it is found that the fitted maximum and minimum water vapor values during a year are always lower than the MERSI PWV ones, but the MERSI PWV values in other months are very close to the predicted ones, which illuminates that the quadratic polynomial function is able to reflect approximately the monthly variation tendency of water vapor over the Tibetan Plateau. It should be noted that the MERSI monthly water vapor product shows a decreasing tendency with time as seen in Figure 5; this is possibly due to the degeneration of sensor, because the values of MERSI monthly water vapor product are much lower after February 2015 and FY-3A/MERSI does not work after 10 March 2018.

3.3. Impact of Topographic Factors on Water Vapor. The research showed that topographic factors could affect the spatial distribution of atmospheric water vapor [10]. There is very high elevation and complex terrain in the Tibetan Plateau. In order to analyze the influence of topographic factors on the distribution of water vapor, MERSI monthly water vapor product is carried out the correlation analysis with the elevation, slope, aspect, latitude and longitude in the Tibetan Plateau, respectively. Firstly, the topographic factors, including elevation, slope, and aspect are resized to a 5 km resolution to match the MERSI monthly water vapor product, and the number of all the pixels within the image of MERSI and topographic factors is 2524677. Then, the correlation analysis is carried out for all the pixels between MERSI monthly water vapor product from February 2010 to September 2015 and each topographic factor (included the longitude and latitude at each pixel), respectively. Finally, the time series chart (Figure 6) of the correlation coefficient between topographic factors and water vapor is shown. As can be seen from Figure 6, the elevation and latitude are negatively correlated with water vapor, which indicates that the water vapor content gradually decreases with increasing elevation and latitude. The correlation between the elevation and water vapor is the best, R is between -0.258 and -0.725, and displays a certain seasonal variation. The best relationship appears in summer with an R of -0.725 and the worst one in winter with R of -0.258. This is mainly due to two possible reasons: the higher the elevation is, the shorter atmospheric water vapor vertical column is, thus the lower the PWV content would be; the difference of air temperature in different seasons results in the distinct evaporation of water vapor over the surface. Since the air temperature is high in summer, the water vapor near surface evaporates quickly; hence, the PWV in the short atmospheric column in the area of high elevation varies considerably. The latitude of the Tibetan Plateau is between 25 and 40° N and the correlation coefficient ranges from -0.110 to -0.391 with water vapor

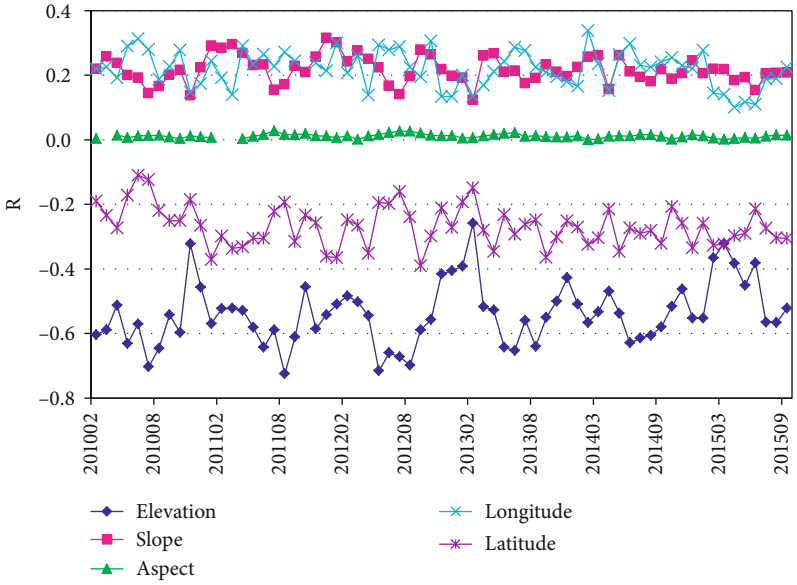

Figure 6: Time series chart of correlation coefficient between topographic factors and water vapor in the Tibetan Plateau.

content. Since the number of samples is 2524677 for all the pixels in the whole image, the minimum R is faithfully obtained at 99% significant level checked with correlation test. The solar incident angle and duration of sunshine always vary with changing latitudes. The higher the latitude is, the shorter the duration of sunshine is. When the land surface receives smaller amount of solar radiation, the water vapor in the surface will be evaporated less. In the south of the Tibetan Plateau, the atmospheric water vapor content is very high, where is situated in low latitude with rich moisture and heat. Bannon et al. [32] also confirmed that water vapor in the northern hemisphere decreased with increasing latitudes from the equator to the North Pole. There is a positive correlation between the slope, longitude, and water vapor in the Tibetan Plateau. The correlation coefficients are between 0.124-0.315 and 0.100-0.337, respectively, and they also reach a 99% significant level due to the large number of samples, but the seasonal variation of the correlation coefficient is not obvious. The slope in the Tibetan Plateau is mainly between 0 and 35° (Figure 2(a)). As the slope increases, the incident angle between the sunshine and the ground enlarges, and the solar radiative effective area increases, then the ground surface is able to receive more solar radiation, so water vapor in the surface is evaporated quickly, which results in the increase of atmospheric water vapor content. The longitude of the Tibetan Plateau stretches across from 70 to 105° E, which has a significant positive correlation with the atmospheric water vapor. Along the longitude from west to east, there is transportation of the water vapor from the Yellow Sea and the East China Sea in the east of China, thus, a gradual increase in the water vapor. The aspect of the Tibetan Plateau varies between 0 and 360° (Figure 2(b)) and the aspect of 0-22.5° or 337.5-360° is defined as ubac, 22.5-112.5° or 247.5-337.5° as semiubac, 112.5-157.5° or 202.5-247.5° as semiadret, and 157.5-202.5° as adret [33]. The aspect can also influence the distribution of solar radiation in the ground surface. Seen from the Figure 2(b), the ubac and adret areas are not significantly distinct, and the correlation coefficient between aspect and water vapor in the whole Plateau is very low around 0.01, which shows that the aspect has the weak effect on the water vapor over the Tibetan Plateau.

4. Conclusion

Based on the validation of MERSI 5-minute water vapor product over the Tibetan Plateau, this paper analyzes the spatiotemporal distribution characteristic of water vapor and discusses the effects of terrain on water vapor over the Tibetan Plateau. The following results were obtained:

(1) Compared with the water vapor data from MODIS, ground-based GPS, and AERONET sun photometer, the MAPE of FY-3A/MERSI water vapor product is in the range of 28.91% -37.54%, the RMSE ranging from 1.87 to 2.76 mm, and the MB between -1.14 and 0.64 mm; MERSI water vapor product displays the best agreement with GPS water vapor data, second with AERONET water vapor data, then with MODIS water vapor product, which shows that MERSI water vapor product has a good accuracy over the Tibetan Plateau

(2) The distribution of water vapor over the Tibetan Plateau displays a certain spatial pattern, that is, the water vapor content is highest in southern Tibet, followed by the eastern, and then PWV content gradually decreases with the increase of elevation from the east to the west. That is, it is high in the northern Qaidam Basin and the southern margin of the Tarim Basin with low elevation. The seasonal variation of water vapor over the Tibetan Plateau is obvious. The PWV content is lowest in winter for 0.57-6.60 mm. Spring and autumn are the transitional

seasons of winter and summer, with spring having 1.20-6.80 mm, while the PWV content in autumn has high values of 1.55-10.00 mm, and that in summer is the highest for 2.40-12.50 mm. The annual water vapor over the Tibetan Plateau presents a periodic variation and accords with the quadratic polynomial law

(3) The topographic factors of the Tibetan Plateau have a certain impact on the water vapor. The elevation and latitude were negatively correlated with water vapor, indicating that the PWV content is decreased with elevation and increasing with latitude. The slope and longitude are positively correlated with water vapor, while the aspect does not have a significant effect on water vapor

Data Availability

All the MERSI water vapor products used in this study were available in the FengYun satellite remote sensing data service network (http://satellite.cma.gov.cn/portalsite/default.aspx). The troposphere zenith path delay (ZPD) and relative meteorological data were obtained from the Scripps Orbit and Permanent Array Center (ftp://cddis.gsfc.nasa.gov/). The level 2.0 data of AERONET were derived from the website (http://aeronet.gsfc.nasa.gov/). The MODIS water vapor products (MOD05) were downloaded from the Earth Observing System Data and Information System (http://reverb.echo.nasa.gov/). And the STRM DEM data were taken from the CIAT-CSI SRTM website (http://srtm.csi.cgiar.org).

Conflicts of Interest

The authors declare that they have no conflicts of interest.

Acknowledgments

This research was funded jointly by the Project of Humanities and Social Sciences of the Ministry of Education in China (grant number:16YJCZH021), the construction project of weather modification in the Northwest China from China Meteorological Administration (grant number: RYSY201907), and the research fund of NUIST-UoR International Research Institute (grant number: 1321041901001).The authors thank the FengYun satellite remote sensing data service network, AErosol RObotic NETwork (AERONET), Earth Observing System Data and Information System (EOSDIS), Scripps Orbit and Permanent Array Center (UCSD), and the Shuttle Radar Topography Mission for their data support.

References

[1] S. Zhou, P. Wu, C. Wang, and J. Han, "Spatial distribution of atmospheric water vapor and its relationship with precipitation in summer over the Tibetan Plateau," *Journal of Geographical Sciences*, vol. 22, no. 5, pp. 795–809, 2012.

[2] B. C. Gao, P. Yang, G. Guo, S. K. Park, W. J. Wiscombe, and B. Chen, "Measurements of water vapor and high clouds over the Tibetan Plateau with the Terra MODIS instrument," *IEEE Transactions on Geoscience and Remote Sensing*, vol. 41, pp. 895–900, 2003.

[3] X. Xu, "The effects of sensitive region over Tibetan Plateau on disastrous weather and climate and its monitoring," *Engineering Sciences*, vol. 11, pp. 96–107, 2009.

[4] X. Liu and B. Chen, "Climatic warming in the Tibetan Plateau during recent decades," *International Journal of Climatology: A Journal of the Royal Meteorological Society*, vol. 20, no. 14, pp. 1729–1742, 2000.

[5] Y. Zhang, D. Wang, P. Zhai, G. Gu, and J. He, "Spatial distributions and seasonal variations of tropospheric water vapor content over the Tibetan Plateau," *Journal of Climate*, vol. 26, no. 15, pp. 5637–5654, 2013.

[6] R. D. Cess, G. L. Potter, J. P. Blanchet et al., "Intercomparison and interpretation of climate feedback processes in 19 atmospheric general circulation models," *Journal of Geophysical Research*, vol. 95, no. D10, pp. 16601–16615, 1990.

[7] M. Bevis, S. Businger, T. A. Herring, C. Rocken, R. A. Anthes, and R. H. Ware, "GPS meteorology: Remote sensing of atmospheric water vapor using the global positioning system," *Journal of Geophysical Research*, vol. 97, no. D14, pp. 15787–15801, 1992.

[8] R. N. Halthore, T. F. Eck, B. N. Holben, and B. L. Markham, "Sun photometric measurements of atmospheric water vapor column abundance in the 940-nm band," *Journal of Geophysical Research*, vol. 102, no. D4, pp. 4343–4352, 1997.

[9] P. K. Karmakar, M. Maiti, S. Sett, C. F. Angelis, and L. A. T. Machado, "Radiometric estimation of water vapor content over Brazil," *Advances in Space Research*, vol. 48, no. 9, pp. 1506–1514, 2011.

[10] P. Zhai and R. Eskridge, "Atmospheric water vapor over China," *Journal of Climate*, vol. 10, no. 10, pp. 2643–2652, 1997.

[11] R. Kistler, E. Kalnay, W. Collins et al., "The NCEP–NCAR 50-year reanalysis: monthly means CD-ROM and documentation," *Bulletin of the American Meteorological Society*, vol. 82, no. 2, pp. 247–267, 2001.

[12] Y. Kaufman and B. Gao, "Remote sensing of water vapor in the near IR from EOS/MODIS," *IEEE Transactions on Geoscience and Remote Sensing*, vol. 30, no. 5, pp. 871–884, 1992.

[13] B. C. Gao and Y. J. Kaufman, "Water vapor retrievals using Moderate Resolution Imaging Spectroradiometer (MODIS) near-infrared channels," *Journal of Geophysical Research*, vol. 108, pp. 4389–4398, 2003.

[14] H. Liu, S. Tang, S. Zhang, and J. Hu, "Evaluation of MODIS water vapour products over China using radiosonde data," *International Journal of Remote Sensing*, vol. 36, no. 2, pp. 680–690, 2015.

[15] H. Liu, S. Tang, J. Hu, S. Zhang, and X. Deng, "An improved physical split-window algorithm for precipitable water vapor retrieval exploiting the water vapor channel observations," *Remote Sensing of Environment*, vol. 194, pp. 366–378, 2017.

[16] J. Liu, H. Liang, Z. Sun, and X. Zhou, "Validation of the Moderate-Resolution Imaging Spectroradiometer precipitable water vapor product using measurements from GPS on the Tibetan Plateau," *Journal of Geophysical Research*, vol. 111, no. D14, 2006.

[17] L. Sun, X. Hu, M. Guo, and N. Xu, "Multisite calibration tracking for FY-3A MERSI solar bands," *IEEE Transactions on Geoscience and Remote Sensing*, vol. 50, no. 12, pp. 4929–4942, 2012.

[18] X. Hu, Y. Huang, Q. Lu, and J. Zheng, "Retrieving precipitable water vapor based on the near-infrared data of FY-3A satellite," *Journal of Applied Meteorological Science*, vol. 22, pp. 46–56, 2011.

[19] B. N. Holben, T. F. Eck, I. Slutsker et al., "AERONET–A Federated Instrument Network and Data Archive for Aerosol Characterization," *Remote Sensing of Environment*, vol. 66, no. 1, pp. 1–16, 1998.

[20] J. Duan, M. Bevis, P. Fang et al., "GPS meteorology: direct estimation of the absolute value of precipitable water," *Journal of Applied Meteorology*, vol. 35, pp. 830–838, 1998.

[21] P. Tregoning, R. Boers, D. O'Brien, and M. Hendy, "Accuracy of absolute precipitable water vapor estimates from GPS observations," *Journal of Geophysical Research*, vol. 103, no. D22, pp. 28701–28710, 1998.

[22] X. Li, G. Dick, C. Lu et al., "Multi-GNSS meteorology: real-time retrieving of atmospheric water vapor from BeiDou, Galileo, GLONASS, and GPS observations," *IEEE Transactions on Geoscience and Remote Sensing*, vol. 53, no. 12, pp. 6385–6393, 2015.

[23] C. Lu, X. Li, T. Nilsson et al., "Real-time retrieval of precipitable water vapor from GPS and BeiDou observations," *Journal of Geodesy*, vol. 89, no. 9, pp. 843–856, 2015.

[24] S. H. Byun and Y. E. Bar-Sever, "A new type of troposphere zenith path delay product of the international GNSS service," *Journal of Geodesy*, vol. 83, pp. 367–373, 2009.

[25] G. Elgered, J. L. Davis, T. A. Herring, and I. I. Shapiro, "Geodesy by radio interferometry: Water vapor radiometry for estimation of the wet delay," *Journal of Geophysical Research*, vol. 96, no. B4, pp. 6541–6555, 1991.

[26] N. Lu, J. Qin, K. Yang, Y. Gao, X. Xu, and T. Koike, "On the use of GPS measurements for Moderate Resolution Imaging Spectrometer precipitable water vapor evaluation over southern Tibet," *Journal of Geophysical Research*, vol. 116, no. D23, 2011.

[27] I. Sano, S. Mukai, M. Yamano, T. Takamura, T. Nakajima, and B. Holben, "Calibration and validation of retrieved aerosol properties based on AERONET and SKYNET," *Advances in Space Research*, vol. 32, no. 11, pp. 2159–2164, 2003.

[28] A. Jarvis, H. I. Reuter, and A. E. Nelson, "Hole-filled seamless SRTM data V4, International Centre for Tropical Agriculture (CIAT)," 2008, available: http://srtm.csi.cgiar.org.

[29] H. Reuter, A. Nelson, and A. Jarvis, "An evaluation of void filling interpolation methods for SRTM data," *International Journal of Geographical Information Science*, vol. 21, no. 9, pp. 983–1008, 2007.

[30] S. Gong, D. F. T. Hagan, X. Wu, and G. Wang, "Spatio-temporal analysis of precipitable water vapour over Northwest China utilizing MERSI/FY-3A products," *International Journal of Remote Sensing*, vol. 39, no. 10, pp. 3094–3110, 2018.

[31] H. Liang, J. Liu, and S. Li, "Analysis of precipitable water vapor source distribution and its seasonal variation characteristics over Tibetan Plateau and its surroundings," *Journal of Natural Resources*, vol. 21, pp. 526–535, 2006.

[32] J. K. Bannon and L. P. Steele, *Average water vapour content of the air, Geophys. Mem., 102*, British Meteorological Office, London, 1960.

[33] Z. Yu, C. Zhang, J. Chen, and C. He, "Topographic correction of sunny and shady slope in different division methods based on slope-matching model," *Journal of Southwest Forestry University*, vol. 37, pp. 178–187, 2017.

Hindawi
Journal of Sensors
Volume 2019, Article ID 8014102, 10 pages
https://doi.org/10.1155/2019/8014102

Research Article

Cross-Sectional Loss Quantification for Main Cable NDE Based on the B-H Loop Measurement Using a Total Flux Sensor

Ju-Won Kim,[1] **Junkyeong Kim**,[2] **and Seunghee Park**[1]

[1]*School of Civil, Architectural Engineering and Landscape Architecture, Sungkyunkwan University, Suwon, Gyeonggi-do 16419, Republic of Korea*
[2]*Research Strategy Team, Advanced Institute of Convergence Technology, Gyeonggi-do 16229, Republic of Korea*

Correspondence should be addressed to Seunghee Park; shparkpc@skku.edu

Received 4 April 2019; Revised 2 July 2019; Accepted 26 July 2019; Published 9 October 2019

Guest Editor: Lalita Udpa

In the real world, the main cables of suspension bridges are commonly inspected by conducting a periodic visual inspection of the exterior cover of the cable. Although there is a need to conduct a nondestructive evaluation (NDE) of the damage of the main cable, a suitable NDE technique has not yet been developed due to the large diameter and low accessibility of the cable. This study investigates a magnetic sensing cross-sectional loss quantification method that can detect internal and external damage to the main cables. This main cable NDE method applies an extremely low-frequency alternating current (ELF-AC) magnetization method and search coil sensor-based total flux measurement. A total flux sensor head consists of a magnetization yoke and a search coil sensor. To magnetize the main cable, a magnetic field was generated by applying a triangular ELF-AC voltage to the electromagnet yoke. The sensing part measures the magnetic flux that passes through the search coil, and the B-H loop was then obtained using the relationship between the ELF-AC voltage that has been input and the total flux that was measured. Also, the cross-sectional loss can be quantified using a variation of magnetic features from the B-H loop. To verify the feasibility of using the proposed NDE technique, a series of experiments were performed using a main cable specimen with a gradual increase in the cross-sectional loss. Finally, the relationship between the cross-sectional loss and extracted magnetic feature was determined and used to quantify the cross-sectional loss via the proposed method.

1. Introduction

In suspension bridges, steel cables are the core supporting materials that suspend most of the load of the structure. However, cross-sectional damage can occur in steel cables due to external causes, including corrosion and fracture. And it can lead to stress concentration as a direct cause of structural failure due the rapid expansion of the damage. Therefore, a suitable nondestructive evaluation (NDE) method is needed to inspect the initial stages of damage in a steel cable so that accidents can be prevented. However, it is difficult to diagnose cables since the damage in cable can be invisible and inaccessible.

To overcome these limitations, this research proposes a noncontact NDE technique incorporating magnetic sensing technology to exploit the ferromagnetic characteristics of steel cables. Magnetic sensors have been extensively used to monitor the safety of structures due to their great reproducibility and reliability [1–3]. Various types of magnetic sensors exist to measure various magnetic properties, and the appropriate magnetic properties obtained from the measured magnetic signals can be used to inspect the structure according to the characteristics of the targeted object [4–7]. Although magnetic sensing techniques have not been commonly used to inspect large-scale civil infrastructure, researchers have recently investigated the use of magnetic sensing methods for large infrastructure, including railroads, pipelines, and suspension bridges [3, 8–10].

Typically, the magnetic flux leakage (MFL) method is an optimal technique for use with continuum structures that have a constant shape in their cross-section, such as railroads and pipelines, and it has been utilized to inspect steel wire ropes for elevators and cranes and for other applications [11–16].

However, the hidden damage within large-diameter cables has not been detected since the MFL technique can only detect a local defect near the surface. Therefore, the MFL method is not a suitable NDE method to inspect the main cables of suspension bridges with a very large diameter. In addition, research and development to replace conventional visual inspection methods have not been actively conducted due to the large size of the main cables.

To overcome such limitations, a new method was proposed to inspect the whole cross-section, including the internal and external section. The proposed technique incorporates an extremely low-frequency alternating current (ELF-AC) magnetization method with total flux measurement using a search coil sensor to obtain magnetic hysteresis loops (B-H loop) according to each condition of the main cable [17]. From the obtained B-H loops, magnetic properties were extracted to quantify the cross-section of the cable, and a quantification algorithm using a variation of the extracted magnetic properties is induced to estimate the rate of cross-sectional loss of the main cables. The feasibility of the proposed main cable NDE technique has been verified through a series of experimental studies using a large-diameter cable specimen with inflicted artificial loss of strands.

2. Theoretical Background

2.1. Magnetization Using an Electromagnetic Yoke. When the material is positioned within a strong external magnetic field, ferromagnetic materials can be magnetized because the magnetic domains within the material are aligned [18]. When a stronger magnetic field is applied to the material, more domains are aligned, and this state is said to be magnetically saturated when all magnetic domains are aligned.

When the solenoid coil is used for the magnetization process, the electric current flows through the carrying conductor in coil; a strong concentrated magnetic field is then generated at the center of the solenoid coil. The strength of the magnetic field in the coil increases as the applied current increases with additional turns of the coil [19]. The magnetic field generated inside the solenoid coil is very helpful to magnetize the ferromagnetic materials to inspect the magnetic domain [9].

However, the magnetization method using a solenoid coil makes it difficult to apply for the continuum specimen in the real field due to its closed-loop shape.

Therefore, a yoke-type electromagnet is utilized in this study to replace the solenoid and improve the applicability in the field. Typically, an electromagnet yoke consists of a solid steel bar core and a solenoid that is winded around the core, as shown in Figure 1.

When an electric current flows through a solenoid around the steel bar, a magnetic flux is exhibited at the steel bar core of the magnetization yoke. When the magnetic flux passes through the magnetization yoke, both ends of the yoke become the north pole and the south pole, respectively. As shown in Figure 1, a magnetic field is then induced between the north and south poles of the yoke.

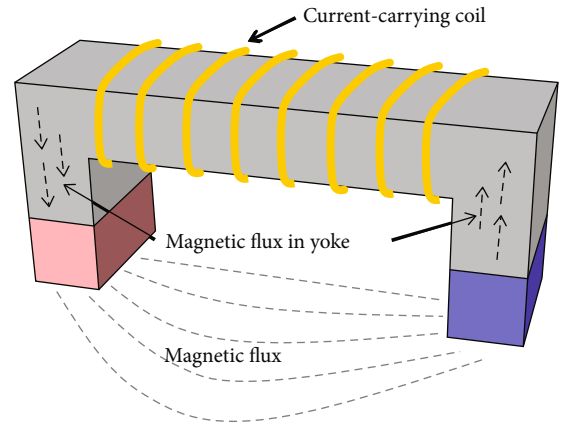

Figure 1: Yoke-type electromagnet for magnetization.

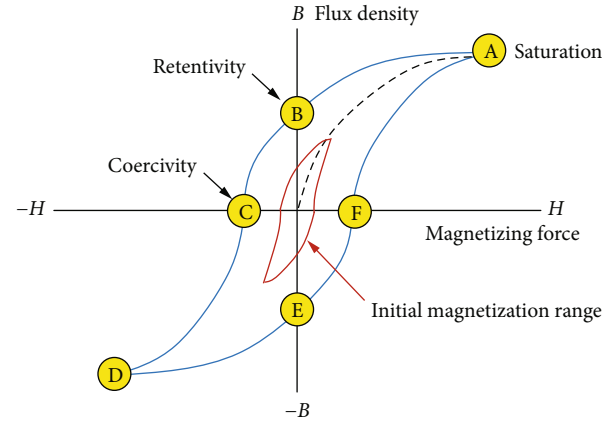

Figure 2: B-H loop (magnetic hysteresis loop) [21].

This magnetic field can be used to indirectly induce a magnetic field in a material so that the specimen can be magnetized for inspection.

In this study, the ELF-AC voltage is applied to magnetize the entire specimen of the main cable using an electromagnetic yoke. The magnetic field produced via ELF-AC can generally penetrate the entire cross-section of the ferromagnetic materials. ELF-AC is very effective when inspecting the entire cross-section of a large specimen because ELF-AC generates an efficient magnetic field that penetrates deeper into the material.

2.2. Search Coil Sensor-Based Total Magnetic Flux Measurement. The principle of the search coil sensing method is based on Faraday's law of induction [4]. A voltage proportional to the rate of variation of the magnetic flux is generated between the leads of the search coil sensor when the magnetic flux through a search coil changes. The magnetic flux through the search coil will vary if the coil moves through a nonuniform field, or if the coil is in a magnetic field that changes with time. The magnetic flux that reflects the condition of the specimen in the magnetic domain is affected by the cross-sectional area of the specimen, material properties, and so on [5].

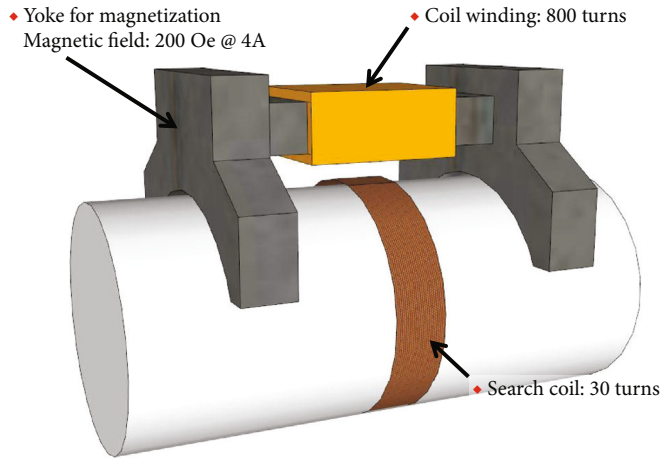

Figure 3: Design of the total flux sensor head.

According to Faraday's law and Lenz's law, the electromotive force generated in a linked search coil by the time variation of the induction is calculated using

$$V_f = -\frac{d\Phi}{dt}, \tag{1}$$

where the total magnetic flux Φ is given as

$$\Phi = NAB, \tag{2}$$

where N is the number of turns of the coil, A is the cross-section of the specimen, and B is the flux density of the specimen.

The magnetic flux density B of the specimen and the induced outer magnetic field H are related as follows:

$$B = \mu_0 \mu_r H, \tag{3}$$

where μ_0 is the related permeability of air and μ_r is the relative permeability of the specimen.

The electromotive force V_f was integrated using the OP amp with the Miller integrator, and the integrated output voltage $V(t)$ is as follows [4, 20]:

$$V(t) = -\frac{1}{RC}\int V_f(t)dt, \tag{4}$$

where RC is the time constant of the integrator. Thus, equation (4) is rewritten as follows:

$$V(t) = \frac{N[\mu_0 \mu_r H]}{RC} A(t). \tag{5}$$

According to equation (5), when the permeability is constant, the output voltage $V(t)$ depends on the cross-section $A(t)$ of the specimen. The output voltage $V(t)$, which is called the total magnetic flux, is measured using a fluxmeter incorporating the OP amp with the Miller integrator.

Table 1: Specification of the total flux measurement system [22].

Search coil diameter	320 mm
Yoke size	$430 \times 440 \times 350$ ($L \times W \times H$) (mm)
Average magnetic path	290 mm
Coil winding	N1: 800 turns, N2: 30 turns
Max current	±14 A
Total flux range	1×10^3 to 2×10^9 Maxwell-turns
Input voltage range	±4 V
Examination time	<60 sec
Magnetizing depth	Entire cross-sectional area
Control program	LabVIEW-based UI

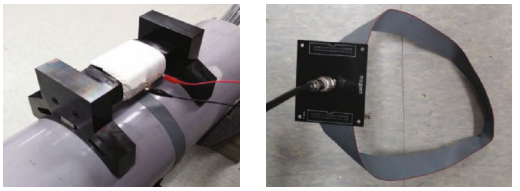

(a) (b)

Figure 4: Fabricated total flux sensor head: (a) magnetization yoke; (b) belt-type search coil sensor.

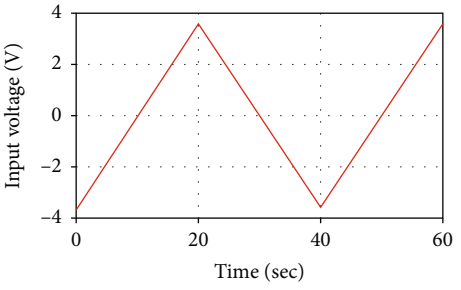

Figure 5: Input voltage shape for magnetization [22].

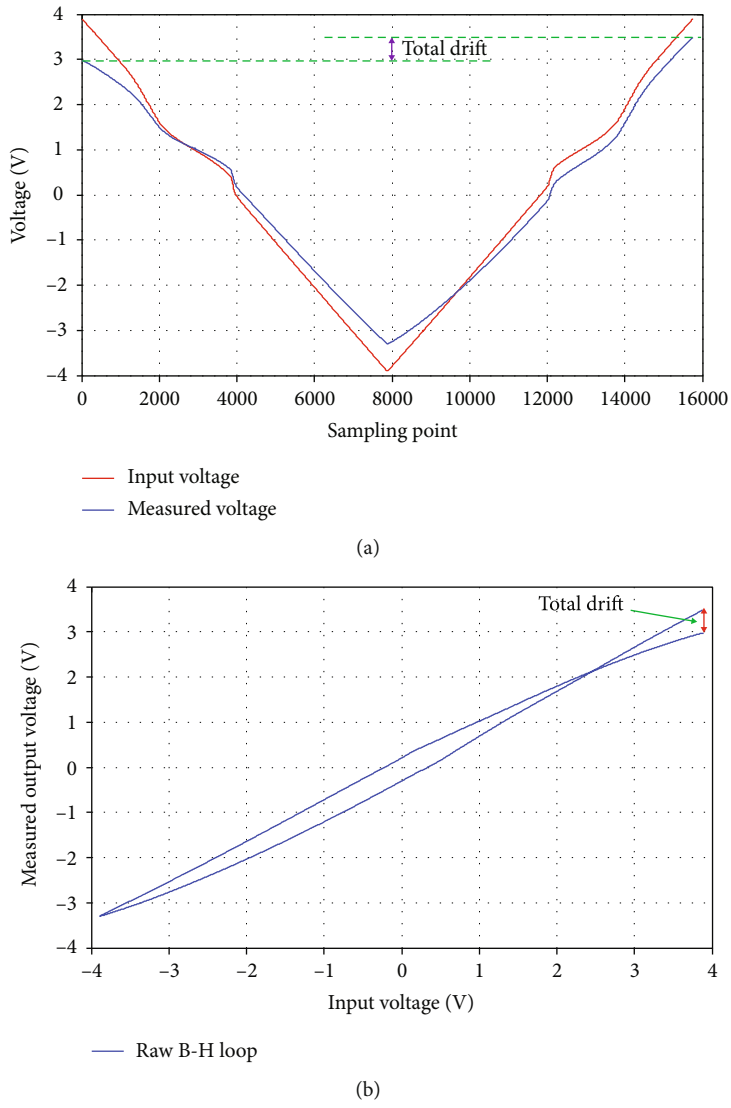

Figure 6: Measured raw signals and raw B-H loop: (a) raw signal; (b) raw B-H loop.

Therefore, the cross-sectional loss can be quantified by measuring the total flux using the search coil sensor and fluxmeter.

2.3. Cross-Sectional Quantification Using a Variation in the Minor B-H Loop. The B-H loop (magnetic hysteresis loop) represents the relationship between the magnetizing force (magnetic field) (H) and induced magnetic flux density (magnetization) (B) [21], as shown in Figure 2.

The B-H loop is obtained by measuring the total flux of a ferromagnetic material while the magnetizing force changes as a cycle. The B-H loop of the whole cycle obtained from a sufficient bipolar magnetic field to make a fully magnetized condition is referred to as a major B-H loop. Utilizing the major B-H loop is the most effective method to conduct the magnetic inspection since the major loop indicates the various magnetic properties of the specimen [21]. However, it is difficult to apply this on site due to the low feasibility since the sensor head required to fully magnetize the real main cable is too big. Therefore, the initial minor B-H loop, the red line in Figure 2, was utilized in this study in place of a major B-H loop to improve the feasibility.

To quantify the cross-sectional loss, the magnetic properties that change according to the cross-sectional loss were extracted. Among the various magnetic properties from the B-H loop, the slope of the B-H loop was extracted and is referred to as the permeability. Permeability is a property of the ferromagnetic material which describes the degree of magnetization of a material in response to a magnetic field. In general, the permeability is used to estimate the tension force of a cable by measuring the voltage from the search coil sensor under the assumption that the constant cross-sectional area is in accordance with equation (5) [4, 20]. Meanwhile, this equation is utilized to estimate the variation in the cross-section $A(t)$ in this study. The cross-section $A(t)$ can be estimated using the measured voltage $V(t)$ when the tension is assumed to be constant.

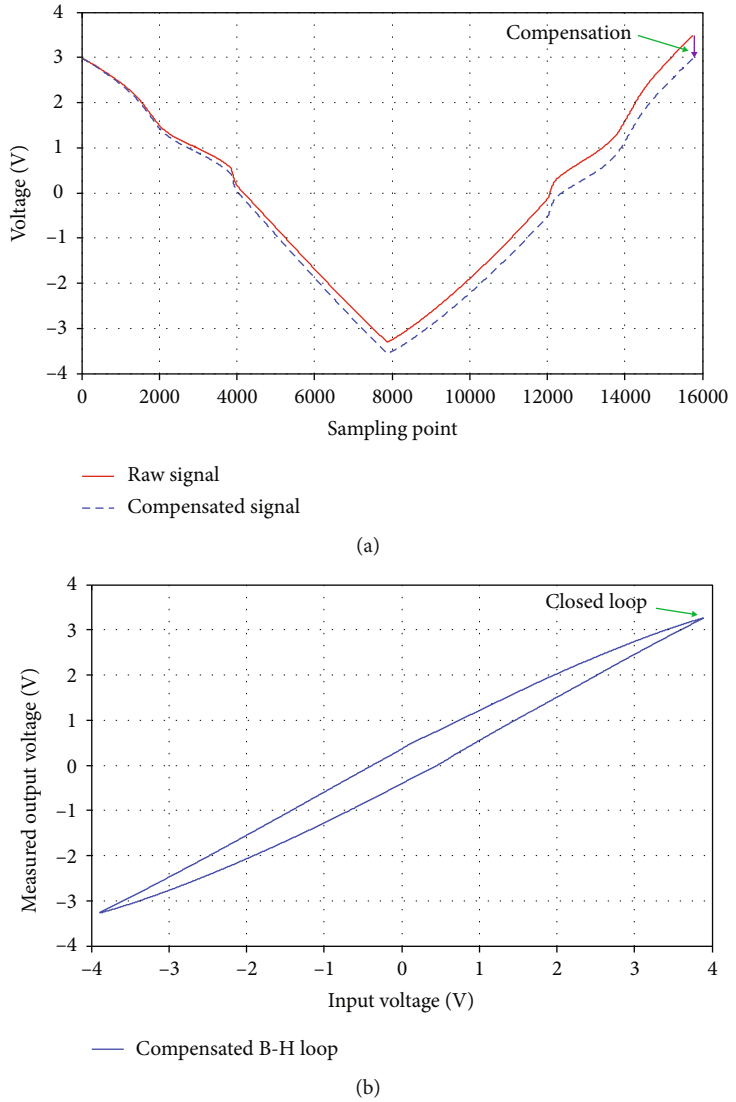

Figure 7: Denoised signal and B-H loop: (a) denoised signals; (b) denoised B-H loop.

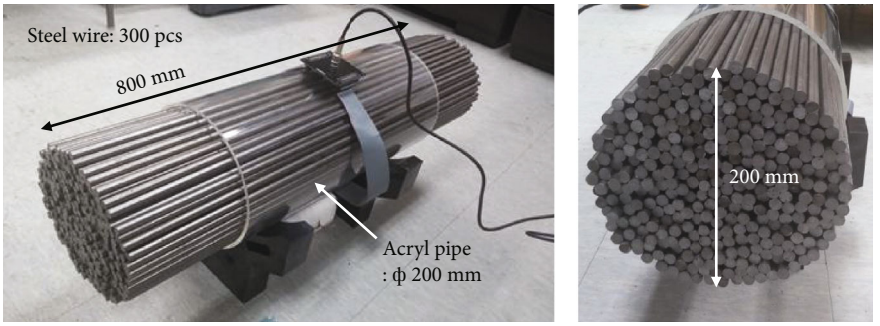

Figure 8: Main cable specimen.

3. System Fabrication for the B-H Loop Measurement

3.1. Fabrication of the Total Flux Sensor Head. Figure 3 shows detailed drawings of the total flux sensor head that was fabricated as described above. It is designed to be suitable for use with a 300 mm diameter main cable. Specific information of the total flux measurement system is described in Table 1.

An electromagnetic yoke consisting of a steel bobbin and a winded solenoid coil is applied to magnetize the large

diameter cable specimen. In addition, the total flux signals were measured using a search coil sensor, and the search coil sensor was configured as an openable belt type using a flexible coil and a PCB board for convenient in situ installation. The fabricated total flux sensor head is displayed in Figure 4.

The magnetization yoke size is 430 mm × 440 mm × 350 mm ($L \times W \times H$), and the coil winding number of the copper coil in the yoke for the magnetization is 800 turns.

The internal diameter of the flexible search coil sensor for sensing the total magnetic flux is 320 mm, and the winding number is 30 turns. The test time for a cycle of the measurement is 60 seconds.

3.2. DAQ Configuration and B-H Loop Acquisition Process. In this system, the ELF-AC voltage is applied to magnetize the entire inside and outside of the specimen. A bipolar power supply generated an ELF-AC voltage, and it is supplied to the primary coil at the electromagnetic yoke to magnetize the main cable specimen.

The cycle of a triangular ELF-AC voltage is supplied to obtain a cycle of the B-H loop in this study. Its amplitude range is ±4 V, and it is supplied to the magnetization yoke for 60 seconds [22]. This voltage can be classified as ELF-AC since it changes very slowly. The wave shape of a triangular ELF-AC voltage applied in the magnetization yoke is shown in Figure 5.

After the magnetizing process, a search coil sensor measures the magnetic flux density from the entire cross-section of the magnetized cable specimen, and the obtained magnetic flux density values are integrated using a fluxmeter to calculate the total magnetic flux.

Since an excessive measurement system is required to obtain a major B-H loop through saturation magnetization of the main cable that has a large size diameter, the voltage range of initial magnetization, shown as the red line in Figure 2, was applied to obtain a minor B-H loop in this study.

Among the characteristics of the B-H loop according to the condition of the cable specimen, the permeability that means the slope of the B-H loop is used to be an index to quantify the variation in the cross-sectional condition.

3.3. Compensation and Denoising Processes to Improve the Quality of the Signals. Figures 6(a) and 6(b) show a sample of the raw signal obtained from the B-H loop. As shown in Figure 6(a), electrical drift occurred during the system operation. This natural drift can disturb the signal and extract the magnetic feature from the B-H loop.

To avoid errors due to drift, a series of denoising processes were performed since the raw signal contains the drift and an offset error. Although this signal processing can induce some distortion in the original B-H loop characteristics, the focus of this study was the index extraction which changes with the cross-section change. Therefore, the following consistent compensation was performed to form the closed B-H loop. This procedure is helpful in providing reference points for index extraction that reflects the B-H loop such as the slope of the B-H loop.

To compensate for the drift error, the total error was divided into a number of sampling points, and the value was added in direct proportion to the sampling point, as shown in Figure 7. In addition, the offset compensation process was performed to facilitate a comparison between the B-H loops from each condition.

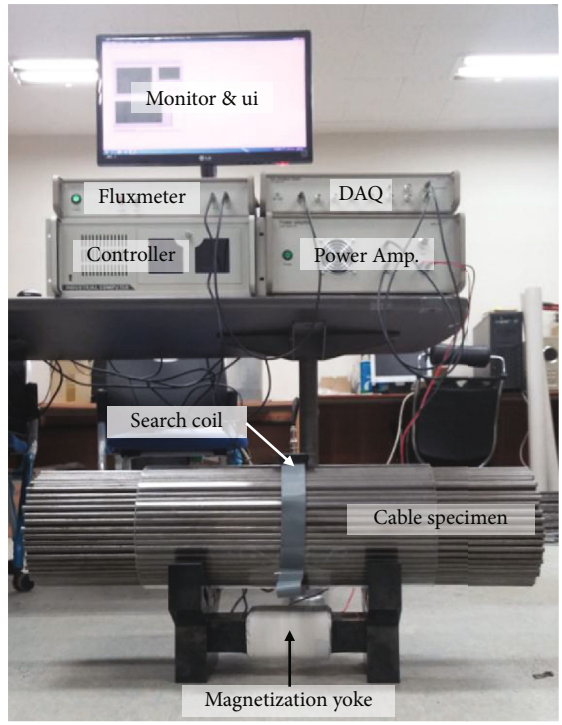

Figure 9: Experimental setup for total flux measurement.

4. Experimental Study

4.1. Experimental Setup and Procedure. A series of experimental studies were performed to examine the capabilities of the cross-sectional loss quantification using the variation of the B-H loop.

A main cable specimen of 200 mm in diameter and 800 mm in length was fabricated for the experimental study, as shown in Figure 8, by filling 300 strands of steel wire in an acrylic pipe-type zig with an internal diameter of 200 mm, as shown in Figure 8. Each strand of the round bar was 10 mm in diameter.

Figure 9 shows the setup for the laboratory experiment. A magnetization yoke and a search coil were installed at the circumferential direction of the specimen. The search coil was fixed to the acrylic case of the specimen when the experiment is carried out since the shape of the search coil can affect the measured signal. A power amplifier to generate the ELF-AC to the wired coil at the magnetization yoke, a fluxmeter to determine the integral of the total flux signal from the search coil sensor, a DAQ, and a controller comprised the measurement system to obtain the B-H loop from the specimen. This measurement system was operated using the LabVIEW user interface.

The test procedure to quantify the cross-sectional loss was the same as that shown in Table 2. To simulate the cross-sectional loss, 30 strands of steel bars were removed

Table 2: Test procedure and steps for the cross-sectional loss.

0% loss	10% loss	20% loss	30% loss	40% loss	50% loss
					

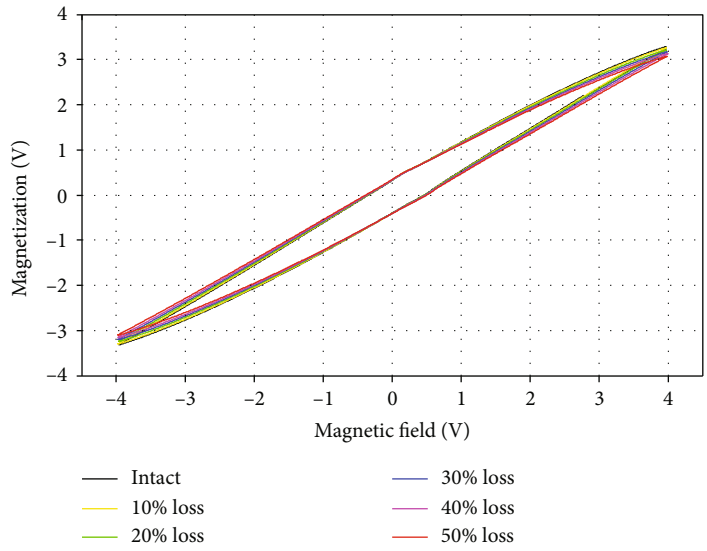

Figure 10: Variation in the B-H loop according to the cross-sectional loss.

at each step from the main cable specimen. Thirty strands of steel bars correspond to 10% of the cross-section of the intact condition, and the experiment was performed in six steps from the intact condition to the 50% loss condition. Using the sensor head and signal measurement system, a cycle of the B-H loop was obtained for a repetition of 10 times in each cross-sectional loss level.

5. Experimental Results

A minor B-H loop from the main cable specimen is obtained at each step of the cross-sectional loss by a cycle of the total flux acquisition and denoised process. The obtained B-H loops using the average value of each case are displayed in Figure 10.

As shown in Figure 10, the dead end of the B-H loops changed gradually. Figure 11 shows the enlarged figure of the dead end of the B-H loops, and it shows that the vertex of the B-H loop decreases progressively, according to the cross-sectional loss level, due to the removal of steel bars.

The variation in the B-H loop implies a variation in various magnetic characteristics according to the specimen's condition, such as permeability, conductivity, and retentivity. Therefore, feature extraction of the magnetic characteristic from the B-H loop is needed to quantify the cross-sectional loss. In this study, the slope of the B-H loop, which means the permeability, was extracted from the B-H loops for each step.

The slope derived from the B-H loop is plotted in Figure 12. The slope of the B-H loop decreases gradually according to the cross-sectional loss, as shown in Figure 12. In addition, the rate of decrease increased slightly, and this was presumed based on the nonconstant magnetization strength due to the biased position of the magnetization yoke.

To improve the accuracy of the damage detection, the cross-sectional loss level between each step was reduced to 1.67%. Figures 13 and 14 show the variation in the B-H loops and the variation curve of the slope of the B-H loop, respectively.

As shown in Figures 13 and 14, the slope decreases with the cross-sectional loss, as with the case of the 10% reduction, and this result shows that a cross-sectional loss of less than 2% can be detected.

In addition, the change in the relation curve in Figure 14 is similar to the change in the range of 0% to 10% of the curve in Figure 12. Therefore, the data sets obtained through the two cases of experiments are seen to have reliability through similarity between the data sets.

These results indicate that the proposed cable inspection method using the total flux sensor can quantitatively diagnose the cross-sectional loss of the large-diameter cable.

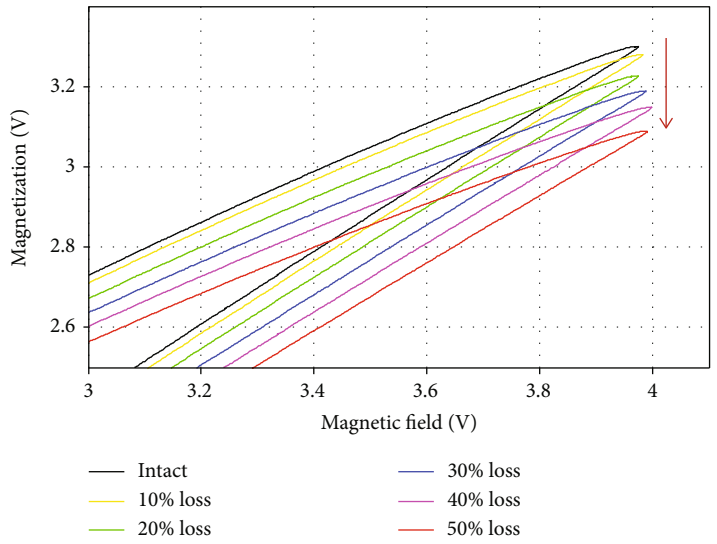

Figure 11: Enlarged plot of the dead end of the B-H loops.

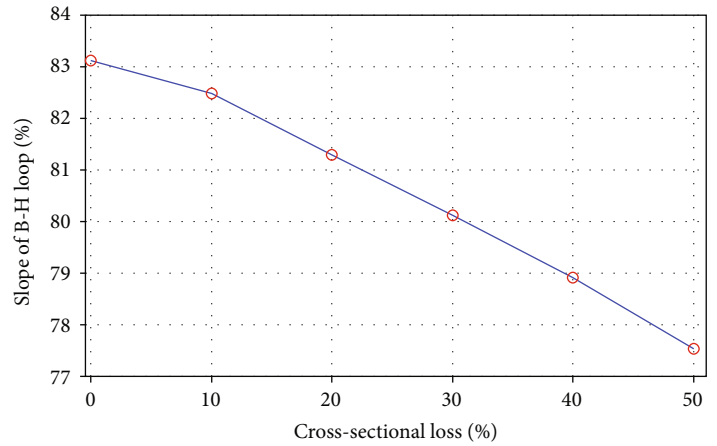

Figure 12: Relation between the extracted feature and the cross-sectional loss.

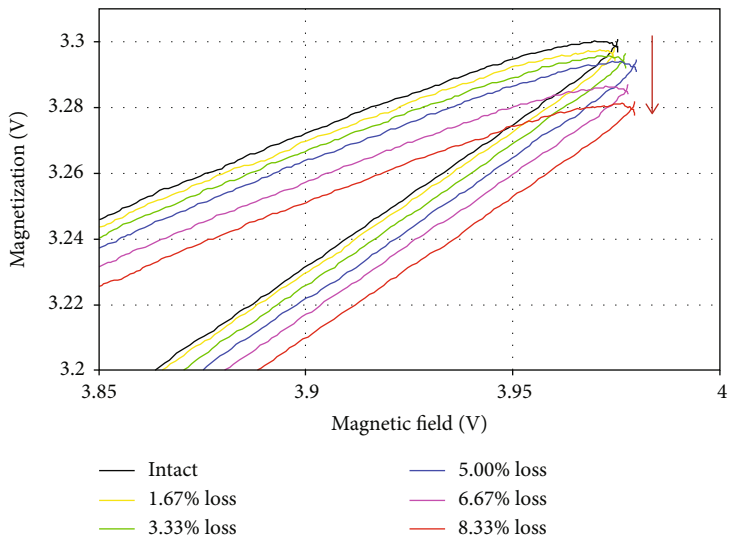

Figure 13: Enlarged plot of the dead end of the B-H loops of the 1.67% reduction case.

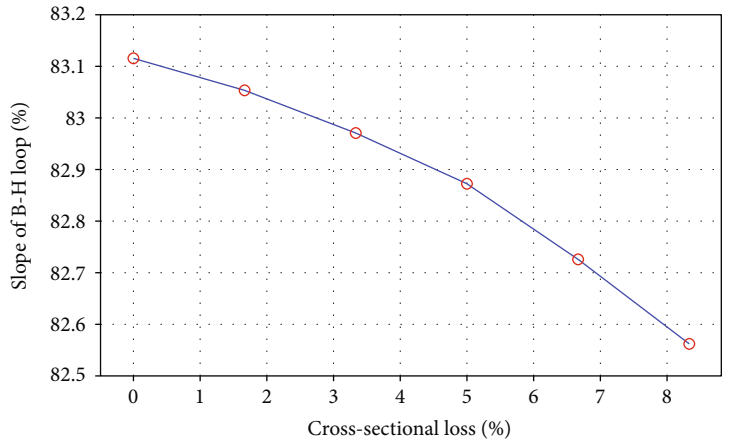

Figure 14: Relation between the extracted feature and cross-sectional loss of the 1.67% reduction case.

6. Conclusions

A main cable NDE method is proposed incorporating ELF-AC magnetization using an electromagnet yoke with a total flux measurement via a search coil to diagnose the cross-sectional loss of the main cable in suspension bridges. A magnetic sensor head for the total flux measurement was fabricated incorporating an electromagnet yoke and a search coil sensor to obtain a B-H loop from the main cable. A series of experimental studies were performed using the fabricated total flux sensor head and the main cable specimen that can remove part of the wire. For each cross-sectional loss level, a B-H loop according to the cross-sectional loss is obtained by using the relationship between the input ELF-AC voltage signal and the measured total flux signal. The slope of the B-H loop, which reflects the permeability, was extracted at each obtained B-H loop to quantify the variation in the B-H loop. This experimental result shows that the slope of the B-H loop decreases gradually according to the stepwise cross-sectional loss and also shows that a constant relationship exists between the variation of the B-H loop and the cross-sectional loss of the main cable specimen. The total flux sensing-based main cable NDE technique can be utilized to diagnose cross-sectional loss without the need for complex destructive testing by obtaining only the B-H loop using a total flux measurement system. This total flux-based main cable NDE technique can be an effective inspection tool to ensure the safety of cable-stayed structures through further research and through the convergence of robots and IT technology.

Data Availability

The raw data of the total flux signal used to support the findings of this study are available from the corresponding author upon request.

Conflicts of Interest

The authors declare that there is no conflict of interest regarding the publication of this paper.

Acknowledgments

This research was supported by the Basic Science Research Program through the National Research Foundation of Korea (NRF) funded by the Ministry of Education (NRF-2017-R1A6A3A04011933 and NRF-2017-R1A2B3007607).

References

[1] K. K. Tandon, "MFL tool hardware for pipeline inspection," *Materials Performance*, vol. 36, no. 2, pp. 75–79, 1997.

[2] C. Mandache, B. Shiari, and L. Clapham, "Defect separation considerations in magnetic flux leakage inspection," *Insight*, vol. 47, no. 5, pp. 269–273, 2005.

[3] M. L. Wang, Z. Chen, S. S. Koontz, and G. D. Lloyd, "Magnetoelastic permeability measurement for stress monitoring in steel tendons and cables," in *Proceedings Volume 3995, Nondestructive Evaluation of Highways, Utilities, and Pipelines IV*, pp. 492–500, Newport Beach, CA, USA, 2000.

[4] J. E. Lenz, "A review of magnetic sensors," *Proceedings of the IEEE*, vol. 78, no. 6, pp. 973–989, 1990.

[5] J. Lenz and S. Edelstein, "Magnetic sensors and their applications," *IEEE Sensors Journal*, vol. 6, no. 3, pp. 631–649, 2006.

[6] K. Mandal and D. L. Atherton, "A study of magnetic flux-leakage signals," *Journal of Physics D: Applied Physics*, vol. 31, no. 22, pp. 3211–3217, 1998.

[7] E. Ramsden, *Hall-Effect Sensors: Theory and Applications*, Elsevier, Newnes, Oxford, UK, 2006.

[8] S. Sumitro, A. Jarosevic, and M. L. Wang, "Elasto-magnetic sensor utilization on steel cable stress measurement," in *The First fib Congress, Concrete Structures in the 21th Century*, pp. 79–86, Osaka, Japan, 2002.

[9] M. L. Wang, G. Wang, and Y. Zhao, *Sensing Issues in Civil Structural Health Monitoring*, Springer, Dordrecht, Netherlands, 2005.

[10] H. R. Weischedel, "The inspection of wire ropes in service: a critical review," *Materials Evaluation*, vol. 43, no. 13, pp. 1592–1605, 1985.

[11] D. L. Atherton, "Magnetic inspection in key to ensuring safe pipelines," *Oil and Gas Journal*, vol. 87, no. 2, 1987.

[12] M. Goktepe, "Non-destructive crack detection by capturing local flux leakage field," *Sensors and Actuators A: Physical*, vol. 91, no. 1-2, pp. 70–72, 2001.

[13] J.-W. Kim and S. Park, "Magnetic flux leakage sensing and artificial neural network pattern recognition-based automated damage detection and quantification for wire rope non-destructive evaluation," *Sensors*, vol. 18, no. 2, pp. 109–119, 2018.

[14] H. R. Weischedel and C. R. Chaplin, "Inspection of wire ropes for offshore applications," *NDT & E International*, vol. 24, no. 6, pp. 323–367, 1991.

[15] S. Park, J.-W. Kim, C. Lee, and J. J. Lee, "Magnetic flux leakage sensing-based steel cable NDE technique," *Shock and Vibration*, vol. 2014, Article ID 929341, 8 pages, 2014.

[16] J.-W. Kim and S. Park, "Magnetic flux leakage–based local damage detection and quantification for steel wire rope non-destructive evaluation," *Journal of Intelligent Material Systems and Structures*, vol. 29, no. 17, pp. 3396–3410, 2017.

[17] S. Park, J.-W. Kim, and D.-J. Moon, "Non-contact main cable NDE technique for suspension bridge using magnetic flux-based B-H loop measurements," in *Proceedings Volume 9437, Structural Health Monitoring and Inspection of Advanced Materials, Aerospace, and Civil Infrastructure 2015*, San Diego, California, USA, 2015.

[18] C. Kittel, "Physical theory of ferromagnetic domains," *Reviews of Modern Physics*, vol. 21, no. 4, pp. 541–583, 1949.

[19] B. D. Cullity and C. D. Graham, *Introduction to Magnetic Materials*, Wiley-IEEE Press, New Jersey, USA, 2nd edition, 2011.

[20] H. A. Radi and J. O. Rasmussen, "Faraday's law, alternating current, and Maxwell's equations," in *Principles of Physics*, Springer, New York, USA, 2013.

[21] S. Chikazumi, *Physics of Ferromagnetism*, Oxford University Press, Oxford, UK, 1997.

[22] J.-W. Kim, S. Park, and D.-J. Moon, "Noncontact NDE technique for main cables of suspension bridges integrating direct current magnetization with a searching coil-based total flux measurement," *IABSE Symposium Report*, vol. 102, no. 7, pp. 2953–2960, 2014.

Hindawi
Journal of Sensors
Volume 2019, Article ID 5848514, 9 pages
https://doi.org/10.1155/2019/5848514

Research Article

Development of a High-Performance Magnetic Field Sensor and Its Application to a Magnetic Field Visualization System Using the Augmented Reality Technique

Hisahide Nakamura,[1] **Yukio Mizuno**,[2] **and Shrinathan Esakimuthu Pandarakone**[2]

[1]*Research and Development Division, TOENEC Corp., Nagoya 457-0819, Japan*
[2]*Department of Electrical and Mechanical Engineering, Nagoya Institute of Technology, Nagoya 466-8555, Japan*

Correspondence should be addressed to Hisahide Nakamura; hisahide-nakamura@toenec.co.jp

Received 17 May 2019; Revised 23 July 2019; Accepted 30 July 2019; Published 9 September 2019

Guest Editor: Dongfeng He

Two- or three-dimensional visualization of magnetic flux density distribution around sources is quite informative for understanding the field environment intuitively. Measurement of magnetic flux density, as well as positioning of measuring points in space, has to be performed in a short time because temporal variation in the source current results in different field environments. It is also valuable to obtain the frequency spectrum of the magnetic field simultaneously at the time of field measurement, especially for sources generating high-frequency components like inverter-driven equipment. This paper develops a high-performance magnetic field sensor which satisfies the above requirements. And, as an application of it, the magnetic field visualization system using the augmented reality (AR) technique is proposed by combining two sensors: one is a magnetic field sensor described above, and the other is a Kinect sensor which has a skeleton tracking function as position determination.

1. Introduction

Visualization of the magnetic field is an effective measure to understand the field environment intuitively. Some papers treated this topic. For example, an interactive visualization system for fast and easy perception of electromagnetic force and electromagnetic field distribution [1], a real-time visualization system which can provide the drawing of the magnetic field generated by a bar magnet and ferromagnetic material [2], and interactive visualization of electromagnetics for engineering education programs [3] have been proposed.

Quantification of the magnetic field has been made by spot measurements around household appliances [4–6] and power facilities [7–11]. Magnetic flux density and/or its frequency characteristics at measuring points have been reported in these researches, but planar or spatial distribution of magnetic flux density around sources has been scarcely evaluated. One of the reasons is that it is a time-consuming and tedious work to carry out spot measurement many times at various points in space. Another reason is that a short-time measurement is required in some cases because magnetic field distribution is bound to change due to temporal variation of current flowing in sources.

The authors proposed a novel system using Kinect to visualize the magnetic field environment around sources and its effectiveness was confirmed by performing some experiments in the laboratory [12]. The system is unique and promising because spot measurements in space of interest can be carried out in a considerably short time compared with conventional measuring procedures and visualization of field distribution can be achieved. The sensor has a disadvantage that the frequency range is below 1 kHz. In case of the measurement of the magnetic flux density generated from electrical equipment driven by commercial frequency,

this range is acceptable. However, it is unavailable for the measurement of the magnetic flux density generated by inverter-driven electrical equipment.

Some meters are available for measurement of magnetic flux density up to 400 kHz [13, 14]. In these meters, magnetic flux density can be obtained but its frequency spectrum is unavailable. Data have to be recorded in a PC with the dedicated software after transferring them from meters to a PC via a cable. The dimensions of the sensor probe are rather large, which is suitable to obtained magnetic field characteristics around power equipment. The field environment generated by a small source like a household appliance is not necessarily evaluated satisfactorily.

In order to understand the magnetic field environment around household appliances in detail and to propose the new visualization system, in this paper, first, a high-performance magnetic field sensor is developed. The frequency range of the sensor is from 30 Hz to 400 kHz. And this sensor can indicate both the resultant magnetic flux density and its frequency components simultaneously. This sensor enables to store data in an external PC by transferring them with Wi-Fi as well as in a USB memory inserted to the USB port on the front of the detector. Next, as an application of this magnetic field sensor, a magnetic flux density visualization system is developed by using the AR technique. AR is a technology for achieving a more realistic expression, which enables adding information created by a computer on an actual scenery, landscape, etc. This visualization system with the AR technique is realized by combining the developed magnetic field sensor and the Kinect sensor, which has the tracking function. Finally, the usefulness of the visualization system based on the AR technique is verified through some experiments.

2. Development of a Magnetic Field Sensor

2.1. Structure of Specification of the Magnetic Field Sensor. The appearance of the developed magnetic field sensor is shown in Figure 1. This sensor consists of three parts: a detector, a probe, and a switch to trigger measurement. The size of the detector's body is $210(\mathrm{W}) \times 230(\mathrm{D}) \times 90(\mathrm{H})$ mm and the weight including the probe is 2150 g.

The frequency range is from 30 Hz to 400 kHz and the measurement range of the sensor is set from 0.2 to 200 μT. The error of the sensor is designed to be less than 2% and it is confirmed by calibration using a Helmholtz coil.

In the detector, a Raspberry Pi [15] is adopted as a processing computer. The Raspberry Pi is a kind of computer. Though it is very small, various functions and some ports, such as a USB and Ethernet, are equipped. An operating clock of Raspberry Pi is from 900 MHz to 1 GHz, while that of a microcomputer is several 10 MHz. Thus, the Raspberry Pi can perform high-speed calculation compared with the microcomputer in signal processing and processing of the input and output of data.

The power of the sensor is supplied from AC100V or a portable battery for cell phones. Since this detector's body weight is about 2 kg, it can be used as a portable sensor with the battery.

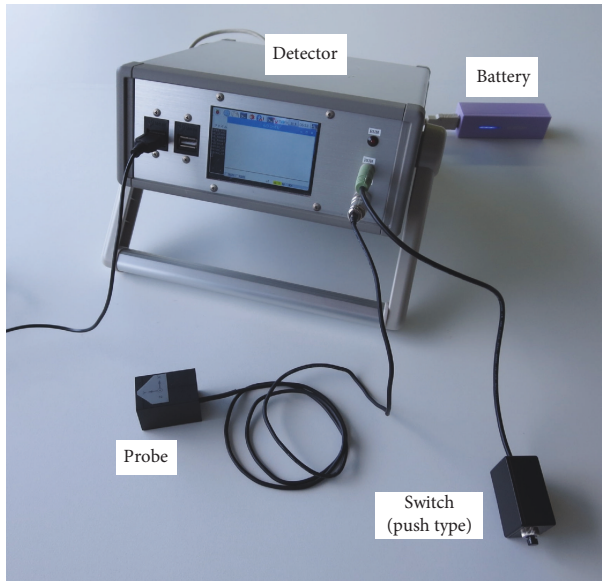

Figure 1: Magnetic field sensor.

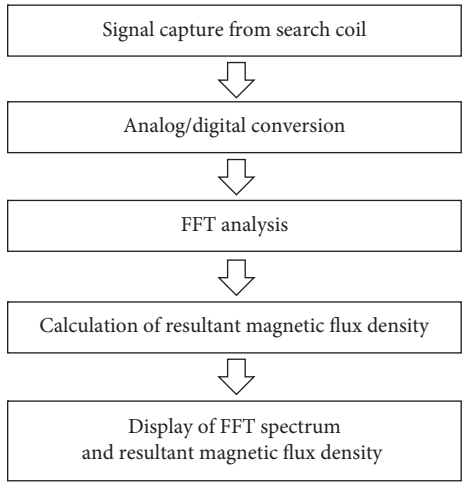

Figure 2: Flow of signal processing of the magnetic field sensor.

Commencement of measurement is triggered by the switch. Two types of switch are prepared: one is a push switch and the other is a toggle switch. The push switch is for one-shot operation, and the toggle switch is for long-time, continuous operation. A user easily selects the switch according to a purpose.

2.2. Signal Processing. The flow of the signal processing of the magnetic field sensor is shown in Figure 2. First, the signal of the magnetic flux density is detected by the probe. It is converted to a digital signal through an A-D converter and is taken in the Raspberry Pi. Raspberry Pi can use a free software: PYTHON. PYTHON is a programming language which has become popular recently in the field of computational science; it has characters that make programming easier and a smaller number of lines than programming language C. In this sensor, the FFT analysis is available with PYTHON. Not only the resultant magnetic flux density but

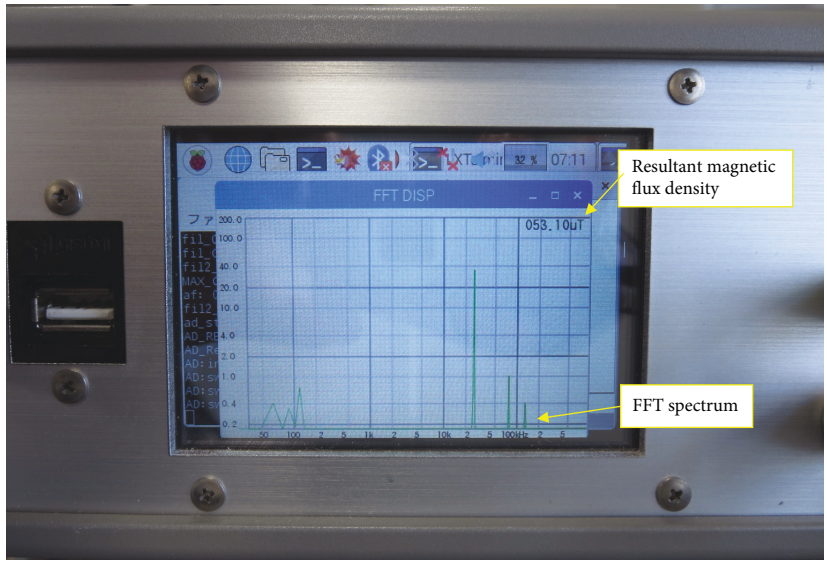

Figure 3: Example of the display.

also its frequency spectrum can be calculated. Finally, both the frequency spectrum and the value of the resultant magnetic flux density are displayed on the LCD of the detector, as shown in Figure 3. In the display of the FFT spectrum, a common logarithm is used in the scale of the horizontal and the vertical axes.

When a USB memory is inserted into the USB port in the front of the detector, Raspberry Pi recognizes it and measured data are saved automatically in a text form. When measurement is repeated, data can also be stored in a hard disk in an external PC by transferring them with Wi-Fi.

3. Visualization System

3.1. Structure of the Visualization System. As an application of the abovementioned magnetic field sensor, the visualization system of the magnetic field is proposed. The structure of the proposed visualization system is shown in Figure 4. It consists of three parts: the magnetic field sensor, a Kinect sensor, and a PC.

The magnetic flux density at various spots is measured by moving the probe. Then, the resultant magnetic flux density and its frequency components are calculated inside the magnetic field sensor. These data are combined into one file and the transmission packet is generated and stored in the specific folder in the Raspberry Pi. Once the PC confirms a file in the specific holder by wireless communication with the sensor, the file is sent to the PC automatically. FFT analysis in the sensor is one of features of the present system, which enables load reduction on the PC during image processing for visualization and indication of the result on a monitor in a short time.

For wireless data transmission between the magnetic field sensor and the PC, both Wi-Fi and Bluetooth are conceivable. Wi-Fi enables a faster communications, better range, and better wireless security than Bluetooth. To achieve the visualization system, a high data transfer rate is required. For this reason, Wi-Fi is adopted in this visualization system. However, Wi-Fi standardly equipped in the Raspberry Pi cannot be used because data transmission is blocked by the detector's case body. In order to avoid this, an external Wi-Fi dongle is used by inserting into the USB port in the front surface of the magnetic field sensor.

3.2. Kinect Sensor [16]. This visualization system of the magnetic field is realized by using a Kinect sensor. A Kinect sensor is one of the motion capture sensors and was released by Microsoft in 2011. It has both an RGB camera and a depth camera and is capable of obtaining information on both the human's skeleton position and the actual background image. Since a Kinect sensor has a function of skeleton tracking, the position of a human's skeleton can be identified continuously by following the movement of the human body. Furthermore, it is inexpensive; the Kinect sensor became familiar among many researchers to analyze the positioning in various fields [17, 18]. Kinect for Windows SDK is also provided as a software development kit. By using Kinect for Windows SDK and based on a depth information obtained from the depth sensor, the human target is extracted as an image. Also, three-dimensional coordinates of his/her 20 joints can be obtained and indicated in the image. Henceforth, both the Kinect for Windows and Kinect for Windows SDK are referred as a Kinect sensor.

The proposed visualization system uses the tracking function of a Kinect sensor. Three-dimensional positional coordinates of the hand are easily obtained. In this system, the position of each measurement point is determined by the position of the hand which holds the search coil.

3.3. Data Processing by PC for Realization of the AR Visualization. The proposed visualization system starts to measure the magnetic flux density after the skeleton tracking Kinect operates. The magnetic flux density at a given measuring point is displayed on a PC screen by various colors depending on its strength. This makes the visualization system based on the AR technique possible.

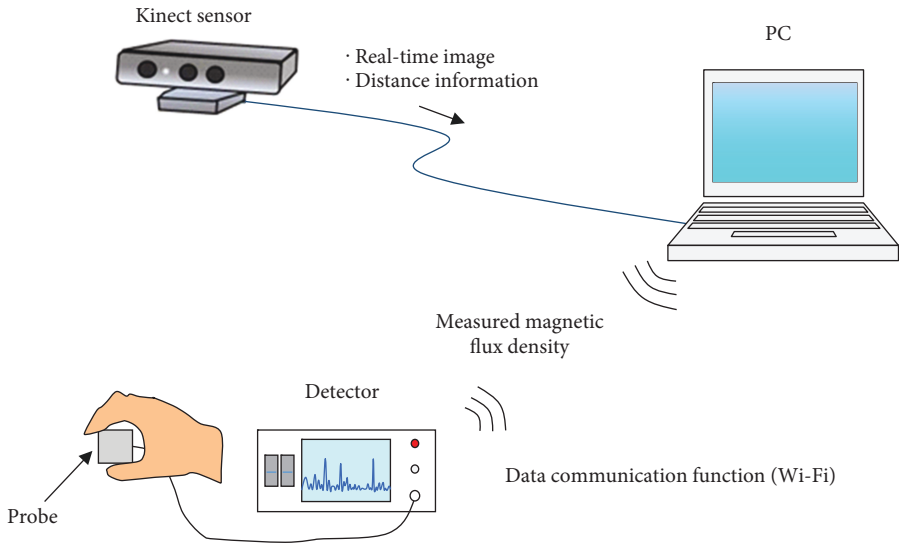

Figure 4: Structure of the visualization system.

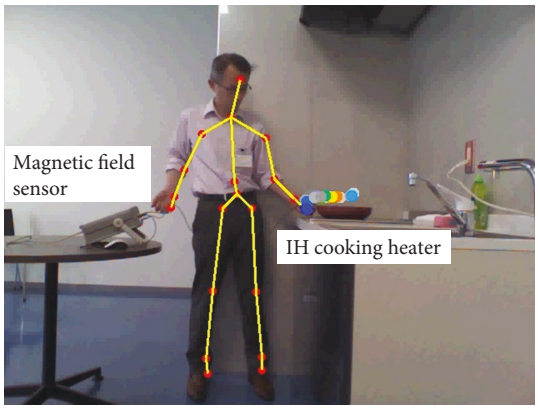

Figure 5: Visualization of the magnetic field of the area around the IH cooking heater.

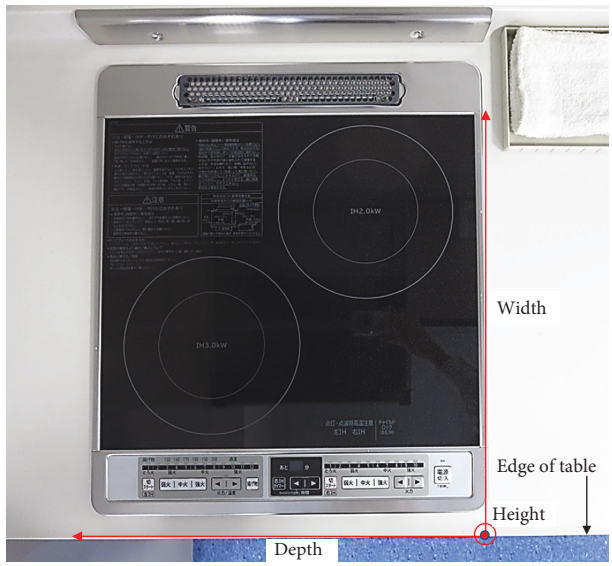

Figure 6: Setting of the coordinate system of IH cooking heater-1.

When the maximum magnetic flux density to be measured is expected to be less than 20 μT, gray and red marks are used to indicate 0 and 20 μT, respectively. Blue, light-blue, green, yellow, and orange marks are allocated to magnetic flux densities between 0 and 20 μT. In the case of indication of magnetic flux density of up to 200 μT, a red mark is allocated to 200 μT and other colors are used similarly to the case of 20 μT. Additionally, gradation is introduced to display the measurement results. The system requires 8 sec for the data acquisition and the indication of a colored mark on the monitor screen.

4. Visualization of Distribution of Magnetic Flux Density

4.1. Visualization of the Distribution of the Magnetic Flux Density around IH Cooking Heater-1. The usefulness of this visualization system is verified through some experiments. In this section, an IH cooking heater is selected as a target equipment. When water in a frying pan is being heated on this IH cooking heater, the magnetic flux density around the cooking heater is visualized. The output of this IH cooking heater is 3.0 kW.

Visualization results of the magnetic flux density displayed on a PC are shown in Figure 5. In this figure, yellow lines and red circles on the body are skeletons and joints, respectively, recognized by Kinect. Magnetic flux density is shown by a color mark as described in Section 3.3; considering the maximum magnetic flux density obtained, red is allocated to 20 μT. The operator holds the probe in his/her left hand and pushes the switch with the right hand. Though the magnetic field sensor is portable, it is put on the desk during this experiment. According to Figure 5, it can be easily realized that a high magnetic flux density is recorded in the area close to the coil of the IH cooking heater. In this way, by utilizing the latest AR technology actively, valuable information can be added to the actual image of a measuring site;

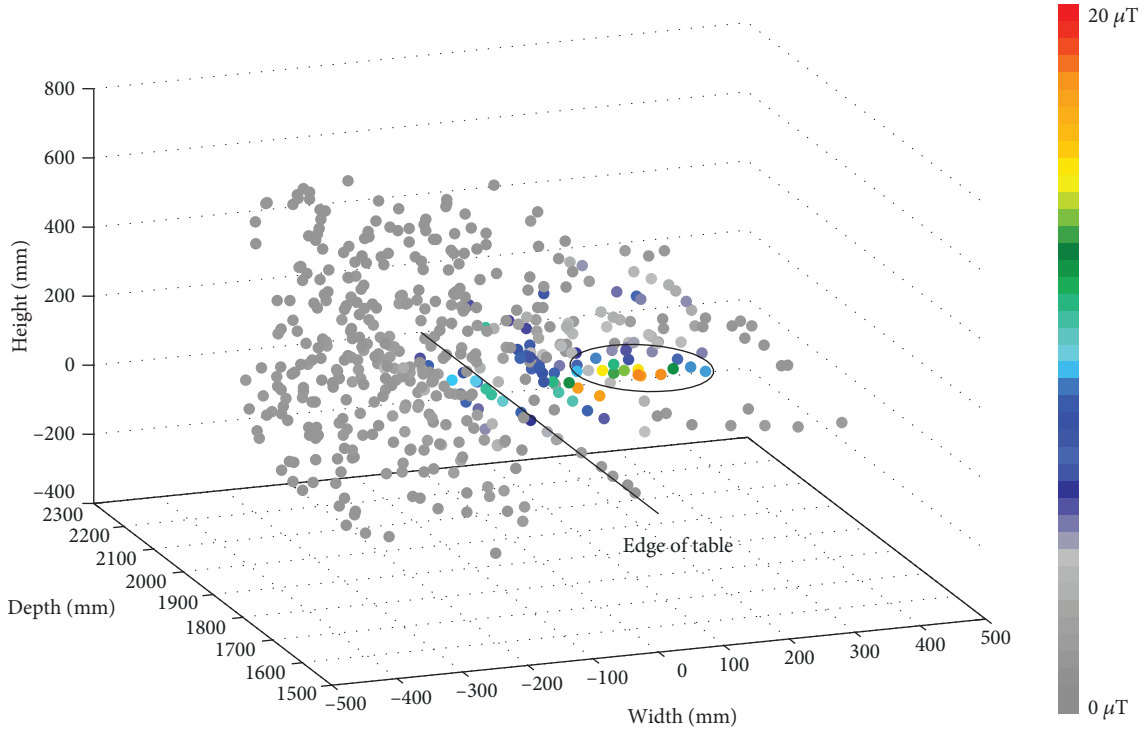

Figure 7: Three-dimensional distribution of magnetic flux density generated by IH cooking heater-1.

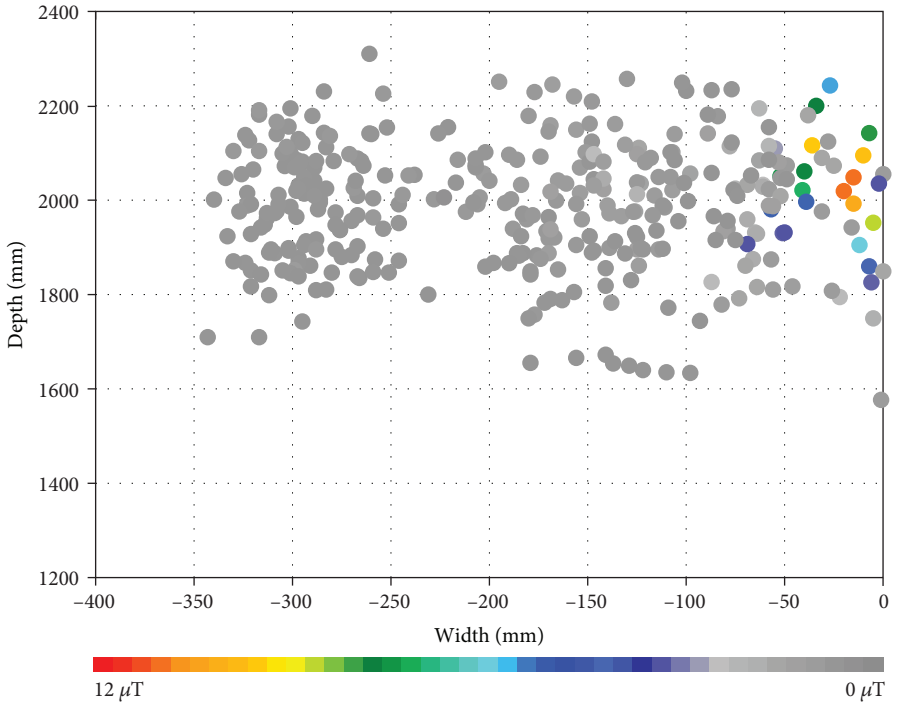

Figure 8: Two-dimensional distribution of magnetic flux density in the area where someone who cooks food stands (width-depth).

it becomes possible to visualize the invisible physical quantities like magnetic field flux density.

As mentioned above, this system can record both the magnetic flux density and the three-dimensional coordinates of the measurement points. The coordinate system is set as shown in Figure 6. "Width" is taken in the direction of the distance from the front of the cooking table toward the back. "Width" is set to be zero at the front of the cooking table. "Height" is taken in the direction of the vertical axis. "Height" is set to be zero at the surface of the cooking table. "Depth" is set in the direction of the distance from the Kinect sensor.

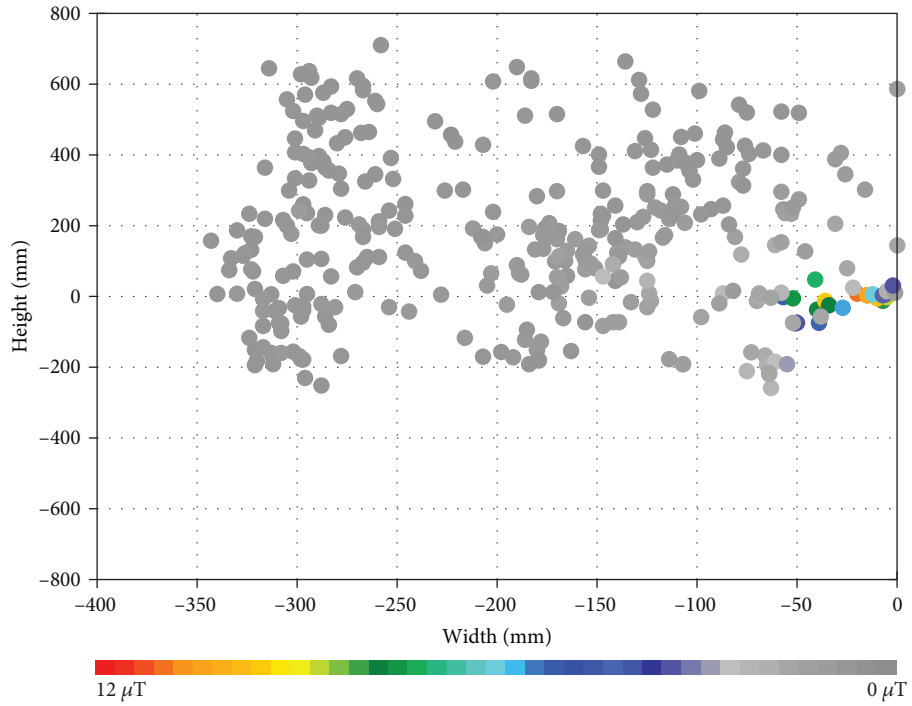

Figure 9: Two-dimensional distribution of magnetic flux density in the area where someone who cooks food stands (width-height).

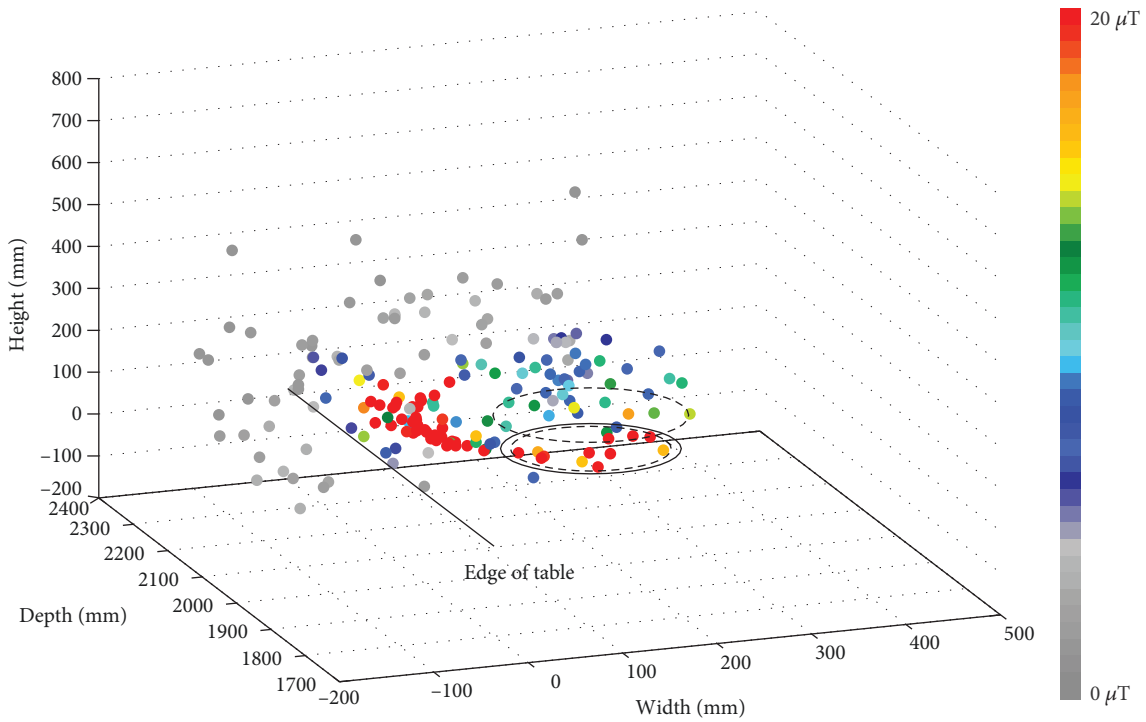

Figure 10: Three-dimensional distribution of magnetic flux density around IH cooking heater-2.

Figure 7 shows the three-dimensional distribution of the magnetic flux density around the IH cooking heater. Magnetic flux density at 492 measurement points is indicated. The circle in this figure means the position of the IH cooking heater. Figure 7 reveals that the magnetic flux density gets smaller as the measuring point leaves from the IH cooking heater.

Furthermore, two-dimensional distribution of the magnetic flux density is shown in Figures 8 and 9. These figures display the magnetic field density obtained in a half space

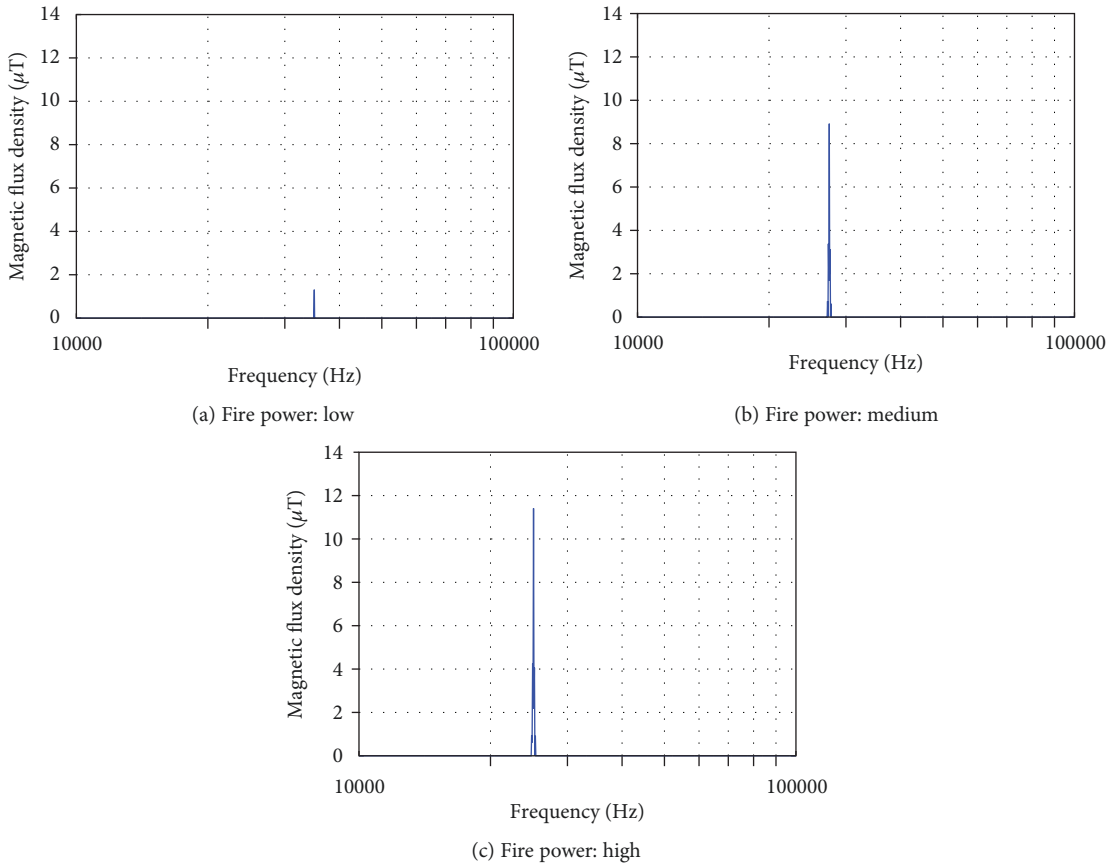

(a) Fire power: low

(b) Fire power: medium

(c) Fire power: high

Figure 11: Change of magnetic flux density and operating frequency depending on fire power.

of negative width (in front of the cooking heater where a cook is expected to stand). The maximum magnetic flux density is less than 12 μT. In order to show distribution of magnetic flux density clearly, in Figures 8 and 9, a red mark is allocated to 12 μT and the gradation display is used depending on magnetic flux density. In Figures 7–9, the distribution of the magnetic flux density around the IH cooking heater can be easily recognized visually; the value is not high in the cooking space.

Magnetic field measurement is carried out at arbitrary spots in the present study, which are located discretely and randomly in space. Thus, the magnetic fields shown in Figures 7–Figure 9 are not consecutive (the same as in Figure 10).

4.2. Visualization of the Distribution of the Magnetic Flux Density around IH Cooking Heater-2. Another IH cooking heater (2.0 kW) is also targeted. This IH cooking heater was manufactured more than 10 years ago and is much older than IH cooking heater-1. A smaller pan is used to fit the coil size of the IH cooking heater, and measurement of magnetic flux density is carried out.

The three-dimensional distribution of the magnetic flux density around IH cooking heater-2 is shown in Figure 10. Magnetic flux density at 492 measurement points is indicated. In this figure, the solid-line circle means the position of the IH cooking heater and two dotted lines mean the upper and lower edges, respectively, of the pan.

According to Figure 10, high magnetic flux density is observed in some points, especially in the area close to the IH cooking heater's plate and the side of the pan. At several points, magnetic flux density exceeds 100 μT. Though the magnetic flux density is high around the IH cooking heater, it is low in the cooking space.

This magnetic field sensor can measure both the magnetic flux density and its frequency components. The frequency spectrum of the magnetic field is available at any point and at any time once turning on the switch connected to the detector's body. This function is valuable especially in the cases when frequency components of magnetic field depend on location and/or time of measurement.

In general, the main operating frequency of the IH cooking heater is between 20 and 50 kHz. The developed magnetic sensor covers the frequency range. It is a potentially powerful tool to investigate characteristics of magnetic flux density during the period that an IH cooking heater starts to operate and reaches the constant fire power.

Figure 11 shows the change of the frequency spectrum in the range of 10 and 100 kHz, which is obtained at the point of the edge of table of the IH cooking heater. It is clearly confirmed that both the frequency component of magnetic flux density and its magnitude change depending on the level of fire power. This is the selling point of the proposed system, which will be especially useful for characterization of magnetic flux density generated by an inverter-fed apparatus/appliance.

Figure 12: Visualization of the magnetic field of the area around the vacuum cleaner.

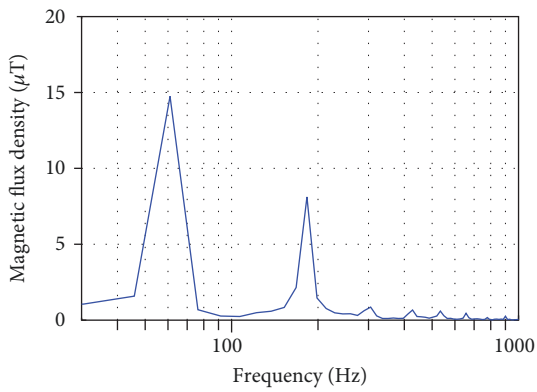

Figure 13: Frequency spectrum of the magnetic flux density measured at the top of the vacuum cleaner.

4.3. Visualization of the Distribution of the Magnetic Flux Density around the Vacuum Cleaner. When the industrial vacuum cleaner is operating with strong suction, the visualization of magnetic flux density around it is performed. The result is shown in Figure 12. This visualization system reveals that the magnetic flux density is strong around the top of the vacuum cleaner and the maximum value is 17.4 μT. Furthermore, the frequency spectrum at the point is shown in Figure 13. According to this figure, it is clear that currents at 60 and 180 Hz are predominant frequencies in this vacuum cleaner.

5. Conclusions

The authors developed a high-performance magnetic field sensor. The frequency band of the sensor is from 30 Hz to 400 kHz; this sensor can calculate both the resultant magnetic flux density and its frequency components simultaneously. They are displayed on the LCD of the detector; measured results are stored in the USB memory inserted into the port on the front of the detector. Raspberry Pi installed in this sensor realizes fast and reliable data transmission via Wi-Fi, visualization of measurement results in a short time, and reduction in cost.

Next, as the application of the magnetic field sensor, the visualization method with the AR technology was proposed. The AR technology is a technique that allows virtual imagery to be combined with the real world. As a core technology, the skeleton tracking function of Kinect is used. Based on this tracking function of Kinect, an inexpensive visualization system was also proposed.

Finally, several experiments were carried out and the distribution of the magnetic flux density was visualized. Moreover, the operating frequency was also identified in a short transient period when fire power of a household appliance changes. This developed magnetic field sensor and the visualization system are particularly expected to be applicable for the analysis and the evaluation of electrical equipment.

However, there are some problems in this system. In regard to the magnetic field sensor, the measurement interval is restricted by the speed of the processing unit of the Raspberry Pi. Acceleration of the processing is necessary to improve the performance of the visualization system. Concerning the visualization system, the skeleton tracking function does not operate correctly when an object exists between the hands holding the probe and the Kinect sensor. Predicting the position of the hand during the tracking function stops is a future work.

Furthermore, as shown in Figures 7–10, there are points where no measurement result is shown. In order to obtain continuous positional distribution of the magnetic field, the magnetic field has to be measured at many points close to each other. The alternative is to calculate the magnetic field at a point without the measured value by interpolation using the magnetic field at adjacent measuring points. This is also a future work.

Data Availability

The data used to support the findings of this study are included within the article.

Conflicts of Interest

The authors declare that they have no conflicts of interest.

References

[1] S. Noguchi, Y. Matsubayashi, H. Yamashita, and V. Cingoski, "A new interactive visualization system with force feedback device in 3-D electromagnetics," *IEEE Transactions on Magnetics*, vol. 40, no. 2, pp. 1382–1385, 2004.

[2] S. Matsutomo, K. Mitsufuji, Y. Hiasa, and S. Noguchi, "Real time simulation method of magnetic field for visualization system with augmented reality technology," *IEEE Transactions on Magnetics*, vol. 49, no. 5, pp. 1665–1668, 2013.

[3] J. Lu, "High performance computation and interactive visualization of electromagnetics for engineering education programs," *IEEE Transactions on Magnetics*, vol. 48, no. 2, pp. 299–302, 2012.

[4] M. Bullo, F. Dughiero, and E. Sieni, "Analysis of stray EM fields generated by induction cooktops," *IEEE Electromagnetic Compatibility Magazine*, vol. 2, no. 2, pp. 49–58, 2013.

[5] Association for Electric Home Appliances, "Measurement of electromagnetic field generated by household appliances (10Hz-400kHz)," 2013, https://www.aeha.or.jp/safety/emwave.html.

[6] M. Iida, Y. Koji, C. Ohkubo, Y. Mizuno, and K. Isaka, *Evaluation of Magnetic Fields Generated by Induction Hob under Assumed Actual Usage Conditions*, PA-101, BioEM, Asilomar, 2015.

[7] I. Magne, F. Audran, E. Mayaudon, D. Clement, and F. Deschamps, "50Hz electric and magnetic field measurements in high voltage substations," in *International Colloquium Power Frequency Electromagnetic Fields ELF EMF, Paper 20*, Sarajevo, 2009.

[8] D. Clement, F. Deschamps, I. Magne, and M. Burceanu, "Inter-Laboratory 50 Hz EMF Measurement," in *BioEM, pp.519-521*, Davos, Switzerland, 2009.

[9] K. Tanaka, Y. Mizuno, and K. Naito, "Measurement of power frequency electric and magnetic fields near power facilities in several countries," *IEEE Transactions on Power Delivery*, vol. 26, no. 3, pp. 1508–1513, 2011.

[10] Y. Miyaji, M. Shimada, Y. Mizuno, and K. Naito, "Evaluation of magnetic field generated by power distribution equipment in accordance with IEC 62110," *IEEJ Transactions on Fundamentals and Materials*, vol. 135, no. 5, pp. 282–286, 2015.

[11] K. Isaka, N. Hayashi, Y. Yokoi, and M. Okamoto, "Characteristics of ground-level electric and magnetic fields generated by ac power transmission lines," *International Symposium on Electromagnetic Compatibility*, vol. 2, pp. 511–514, 1989.

[12] S. E. Pandarakone and Y. Mizuno, "Advanced visualization system of magnetic field distribution using wireless magnetic sensor module and skeleton tracking Kinect," *IEEJ Transactions on Fundamentals and Materials*, vol. 137, no. 1, pp. 46–51, 2017.

[13] "Magnetic Field Hitester," https://www.hioki.com/en/products/detail/?product_key=5582.

[14] "ELT-400, Measuring device for evaluating safety in magnetic fields(1Hz-400kHz)," https://www.narda-sts.us/page.php?ID=10&Z=Low+Frequency+Meters.

[15] https://www.raspberrypi.org.

[16] "Kinect for Windows," https://developer.microsoft.com/en-us/windows/kinect.

[17] H. Miyajima and M. Yamamoto, "Personal identification based on skeletal movement using Kinect," *The Journal of The Institute of Image Information and Television Engineers*, vol. 67, no. 11, pp. J417–J420, 2013.

[18] I. Iimura, Y. Imamura, Y. Kiridoshi, Y. Moriyama, and S. Nakayama, "Self-organizing maps-based Japanese flag signaling recognition by using Kinect," *IEEJ Transactions on Electronics, Information and Systems*, vol. 135, no. 1, pp. 138-139, 2015.